2010-07-08

Modeling, Design, and Testing of Contact-Aided Compliant Mechanisms in Spinal Arthroplasty

Peter Andrew Halverson
Brigham Young University - Provo

Modeling, Design, and Testing of Contact-aided Compliant Mechanisms in Spinal Arthroplasty

Peter A. Halverson

A dissertation submitted to the faculty of
Brigham Young University
in partial fulfillment of the requirements for the degree of

Doctor of Philosophy

Larry L. Howell, Chair
Anton E. Bowden
Spencer P. Magleby
Scott L. Thomson
Kenneth A. Solen

Department of Mechanical Engineering

Brigham Young University

August 2010

ABSTRACT

Modeling, Design, and Testing of Contact-aided Compliant Mechanisms

in Spinal Arthroplasty

Peter A. Halverson

Department of Mechanical Engineering

Doctor of Philosophy

Injury, instrumentation, or surgery may change the functional biomechanics of the spine. Spinal fusion, the current surgical treatment of choice, stabilizes the spine by rigid fixation, reducing spinal mobility at the cost of increased stress at adjacent levels. Recently, alternatives to spinal fusion have been investigated. One such alternative is total disc replacements. The current generation of total disc replacements (TDRs) focuses on restoring the quantity of motion. Recent studies indicate that the moment-rotation response and axis of rotation, or quality of motion (QOM), may have important implications in the health of adjacent segments as well as the health of the surrounding tissue of the operative level.

This dissertation examines the use of compliant mechanism design theory in the design and analysis of spinal arthroplasty devices. Particularly, compliant mechanism design techniques were used to develop a total disc replacement capable of replicating the normal moment-rotation response and location and path of the helical axis of motion. Closed-form solutions for the device's performance are proposed and a physical prototype was created and evaluated under a modified F1717 and a single-level cadaveric experiment. The results show that the prototype's QOM closely matched the selected force-deflection response of the specified QOM profile.

The use of pseudo-rigid-body modeling to evaluate the effects of various changes on motion at adjacent segments is also investigated. The ability to model biomechanical changes in the spine has traditionally been based on animal models, in vitro testing, and finite element analysis. These techniques, although effective, are costly. As a result, their use is often limited to late in the design process. The pseudo-rigid-body model (PRBM) developed accurately predicted the moment-rotation response of the entire specimen and the relative contribution of each level. Additionally, the PRBM was able to predict changes in relative motion patterns of the specimen due to instrumentation.

Keywords: spinal arthroplasty, compliant mechanisms, psuedo-rigid-body model

ACKNOWLEDGMENTS

This work has been supported by a large number of people and organizations to whom I am indebted. Brigham Young University has been generous in their provision of funding, research equipment, facilities, and personnel. This research has been funded in part by Crocker Spinal Technologies.

As with most things, the most valuable contribution that has been given are the personal interactions that have been experienced. The faculty and staff at BYU have provided insight and mentoring during the process. I feel that a deep sense of gratitude should also be expressed to Dr. Howell and Dr. Bowden for their support and direction over the last several years and Dr. Jorge Ochoa for his insights. Kevin Cole and Ken Forester have provided valuable experience in the establishment of our testing facilities and creation of prototypes. Keith Stolworthy and Shannon Zirbel have provided expertise in the physical testing of devices and specimens. Special thanks to Eric Stratton for his help along the way.

Finally, I would like to express my gratitude to my wife, without whom I could not have done any of this.

TABLE OF CONTENTS

LIST OF TABLES

LIST OF FIGURES

NOMENCLATURE

CORE	Compliant Rolling-contact Elements
EMG	Electromyography
FDA	Food and Drug Administration
FEA	Finite-element Analysis
FSU	Functional Spinal Unit
HAM	Helical Axis of Motion
IAR	Instantaneous Axis of Rotation
IVD	Intervertebral disc
LBP	Lower Back Pain
PRBM	Pseudo-rigid-body Model
QOM	Quality of Motion
TDR	Total Disc Replacement

CHAPTER 1. INTRODUCTION [1]

Lower back pain (LBP) will afflict as much as 80% of the adult population at some point during their lifespan [2]. While the exact cause of LBP is difficult to diagnose, it is increasingly common in patients where trauma or age has damaged the functional spinal unit (FSU). Current surgical solutions, such as spinal fusion, alter the biomechanics of the spine and can have adverse effects on adjacent levels. Replication of the proper biomechanical response of the spine is necessary for good long-term clinical results [57, 62–64].

The primary objective of this work is the development of principles and techniques that will provide the basis for the design of a contact-aided compliant-mechanism-based orthopedic device capable of mimicking the biomechanics of the lumbar spine. The tools developed should be capable of producing a device with theoretical wear-free motion. The secondary objective is the development of modeling techniques which may be used in the early-stage design process to model the effects of injury, surgery, and instrumentation on the adjacent spinal levels.

The FSU is the smallest physiological unit of the spinal column that exhibits biomechanical properties similar to those of the entire spine. It is composed of a superior and inferior vertebra, surrounding ligaments, two zygapophyseal (facet) joints, and the intervertebral disc (IVD). An illustration of the FSU is shown in Figure 1.1.

The IVD and facets form a three joint complex that provides multiple functions, including protection of the spinal cord, support and transmission of loads, motion, spinal stabilization, and dampening of impact. Damage to any of these joints results in an adverse change in spinal biomechanics. Biomechanical dysfunction of the spine often leads to neurological deficits and LBP. When the damage becomes sufficient as to warrant operative care, the surgeon must decide which functions of the spine to restore. This restoration may take place through several possible techniques, including spinal arthrodesis (fusion) and spinal arthroplasty.

[1] Portions of this chapter have been published in [1]

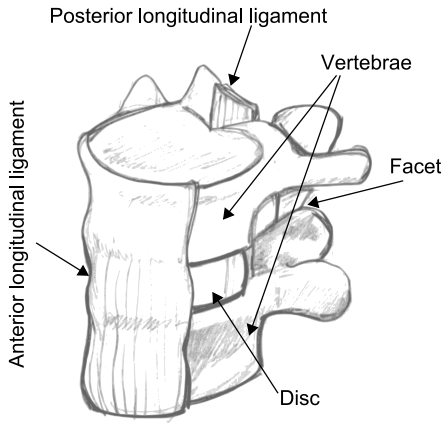

Figure 1.1: The Functional Spinal Unit (FSU).

1.1 Biomechanics of the Lumbar Spine

The spinal biomechanics metrics referenced in this dissertation have been obtained through multiple methods: in vivo, in vitro, and mathematical/computer aided. Each method has its own advantages and disadvantages. In vivo, or studies using living subjects, provide the most accurate loading conditions of the spine. However, there are difficulties inherent with in vivo experimentations, particularly in data acquisition and understanding boundary conditions. In vitro studies are a common alternative. In vitro experiments, studies in a controlled laboratory using part of the organism, are beneficial in that they offer the ability to control the boundary conditions applied to the spine, are easier to instrument, and experiments may be destructive in nature. Finally, computer modeling is often used to predict stresses and loads within the IVD. As computer modeling requires validation from in vivo or in vitro models, data obtained through computer simulation will be explicitly notated.

This section presents the biomechanical properties of the FSU as it pertains to spinal arthroplasty. The primary function of the FSU is to protect the spinal cord. As this function is directly related to the ability of the FSU to resist load, expected forces on the spine are discussed first. The next requirement of the FSU is its ability to allow motion followed by its ability to control the quantity (kinematics) as will as the quality (kinetics) of motion.

Table 1.1: Approximate force on the L3-L4 disc of a 70 kg male [11].

Position/Load	Forces (N)
Awake	250
Upright sitting (no support)	700
110° sitting with back rest	400
Standing	500
Flexed 20°, rotated 20°, 10 kg weight	2100
Holding 5 kg arms extended	1900
Lifting 10 kg, back bent	1900

1.1.1 Forces

There is a wide variation in the reported magnitudes of forces and torques in the lumbar spine. Methods to determine in vivo loading include mathematical models such as static [3, 4] and dynamic calculations aided by electromyography (EMG) measurements [5–7], and/or optimization techniques [3], spinal implants incorporating load sensors, and IVD pressure measurements. Each one of these methods presents distinct advantages and disadvantages [8]. Some of these methods have yielded dramatically different results. An example is that static free-body-diagrams of power lifters have shown that the short-term forces in the lumbar spine may exceed 11,000 N [4]. Yet in vitro studies have shown that failure may occur at much lower forces (1000 N). Possible explanations for this discrepancy are the effects of aging, exercise-related physiologic adaptation of the spinal structures, unknown secondary control mechanisms, non-physiological loading conditions in vitro, or a non-complete static model [4, 9]. This discrepancy emphasizes the need to design the implant in a manner as to avoid failure under a variety of conditions.

Nachemson measured the in vivo intradiscal pressure of the L3-L4 disc [10] by inserting a needle into the disc of a healthy volunteer. Pressure measurements were then taken for multiple positions and loading conditions. Forces were calculated from the disc area. These numbers were later revised to account for a measurement bias [11]. Some of these positions and forces are shown Table 1.1. These experiments were single-subject experiments and somewhat limited, but are generally considered accurate. Similar pressures were confirmed by Wilke et al. in the L4-L5 disc [12].

Table 1.2: Range of motion of the lumbar spine in flexion (forward bending), extension(backward bending), lateral (side to side) bending (left + right) and axial (twisting) torsion.
All units are in degrees.

Level	Flexion	Extension	Lateral Bending	Axial Torsion
L1-2	5.8 ± 0.6 (8-5.6)[a]	4.3 ± 0.5 (5-4.3) [a]	5.2 ± 0.4 (6.0-5.2)[b]	2.6 ± 0.5 (2.6-1)[c]
L2-3	6.5 ± 0.3 (10-6.5) [a]	4.3 ± 0.3 (4.3-3.0) [a]	7.0 ± 0.6 (7.0-6.0) [b]	3.0 ± 0.4 (2.2-1) [c]
L3-4	7.5 ± 0.8 (12-7.5) [a]	3.7 ± 0.3 (3.7-1.0) [a]	5.8 ± 0.5 (5.0-8.0) [b]	2.7 ± 0.4 (2.7-2) [c]
L4-5	8.9 ± 0.7 (13-8.9) [a]	5.8 ± 0.4 (5.8-2.0) [a]	5.9 ± 0.5 (2.0-6.0) [b]	2.7 ± 0.5 (1.7-2) [c]
L5-S1	10.0 ± 1.0 (10.0-9) [a]	7.8 ± 0.7 (7.8-5.0) [a]	5.7 ± 0.4 (2.0-5.7) [b]	1.5 ± 0.2 (1.5-0) [c]

[a] In vivo: [20] In vitro: [21]*
[b] In vivo: [17, 22] In vitro: [21]
[c] In vivo: [22]* In vitro: [21]
*additional estimates from [18]

1.1.2 Range of Motion

Enhancements in imaging technology have led to increased accuracy in range of motion measurements. As a result, a variety of data concerning range of motion is available. The data given in Table 1.2 gives the most probable value, the standard deviation from the study, and the range of values over multiple studies for flexion (forward bending), extension (backward bending), lateral bending (sideways bending), and axial torsion (twisting). Additional studies have combined flexion and extension data [13–19]. These values correspond closely for the lumbar range of motion data given in Table 1.2.

1.1.3 Kinematics

During physiologic motion, the location of the instantaneous axis of rotation changes orientation and location. The path and orientation of the instantaneous axis of rotation over time can be tracked quantitatively, and is referred to as the centrode of motion. Because of the three-joint nature of the FSU, a change in the instantaneous axis of rotation will result in a modified stress [23]. Although some research has studied the centrode [24–28], the instantaneous axis of rotation has been studied in greater depth and is the most widely used method of kinematic analysis in the field. Recent enhancements in imaging technology have made possible improved estimates of the instantaneous axis of rotation for flexion-extension, lateral bending, and axial torsion. These locations are shown in Figure 1.2.

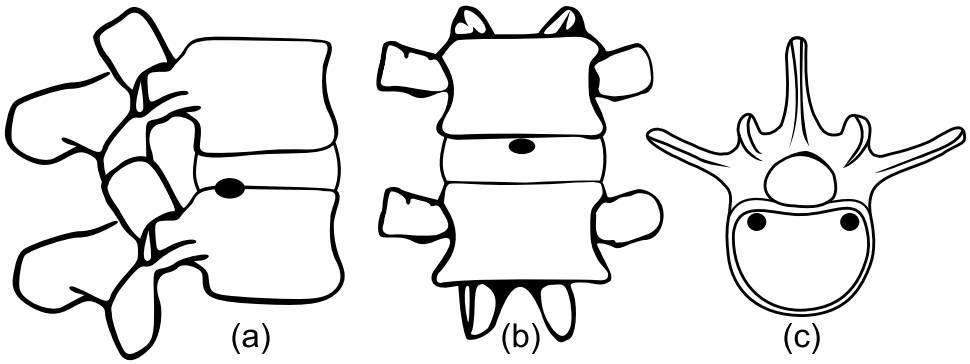

Figure 1.2: Instantaneous axes of rotation for (a) flexion-extension [20], (b) lateral bending [29], and (c) axial torsion [30].

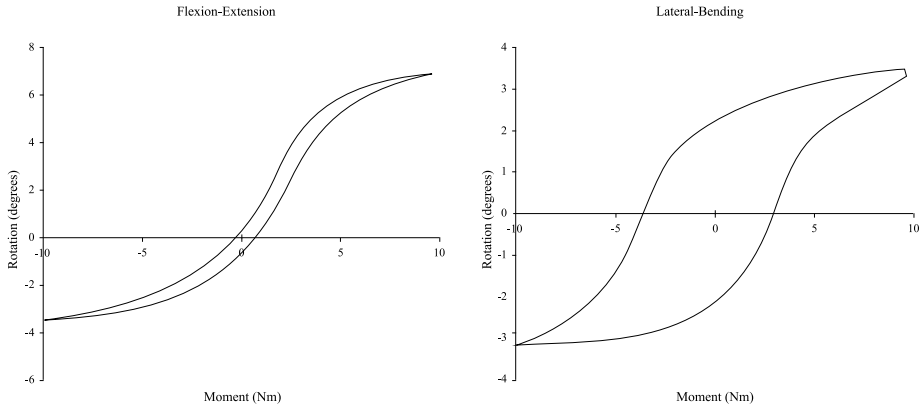

Figure 1.3: Typical force-deflection curves for L4-L5 in flexion-extension and lateral bending [31].

1.1.4 Kinetics

Another unique property of the IVD is that unlike diarthrodic joints, the IVD exhibits a distinct non-linear force-deflection characteristic for flexion-extension and lateral bending. This force-deflection characteristic is believed to be critical to the health of the spine. While the disc's contribution to the overall FSU force response is still unknown, the force-deflection characteristics of the FSU have been measured. A typical force-deflection response exhibits a highly non-linear curve in flexion-extension and lateral bending [31], as shown in Figure 1.3. The exact force-deflection characteristics will be patient dependent, the spinal level, and the health of the FSU. While the force-deflection relationship for axial torsion is slightly non-linear, a linear approximation of 9 Nm/deg is sufficient for most considerations [31].

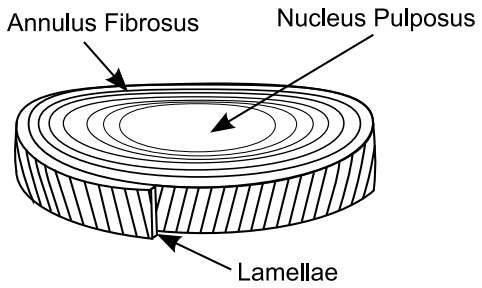

Figure 1.4: The intervertebral disc.

1.1.5 Composition

Unlike diarthrodial joints, such as the knee, where the main resistance to motion is friction, a source of the non-linear force-deflection relationship is the compliance inherent in the construction of the IVD. Although the exact size and shape of the IVD varies throughout the lumbar region of the spine, the disc is roughly the shape of a kidney bean, as illustrated in Figure 1.4. The disc itself is generally discussed in two parts, the nucleus pulposus and the annulus fibrosus. The annulus consists of several concentric layers called lamellae. Each lamella contains parallel collagen fibers aligned 30 degrees from vertical. The fiber orientation alternates between adjacent lamellae. The outer layers of the annulus are analogous to the walls of a pressure vessel. The working fluid of the pressure vessel, collagen fibers in a mucoprotein gel, is called the nucleus. When the disc is loaded in compression, the nucleus exerts a hydrostatic pressure on the outer layers of the annulus, providing stability and flexibility. As the nucleus becomes smaller, either by age or trauma, it loses its ability to provide hydrostatic pressure and the load must be absorbed directly by the annulus [32]. Due to the complexity of the construction, an artificial disc patterned after the exact construction of the natural disc (i.e. alternating the fibers of the lamellae) would be difficult. However, it is hypothesized that mimicking the compliant principles behind the disc is possible through the use of compliant mechanisms.

1.2 Compliant Mechanisms

If a mechanism is defined as a mechanical device that is capable of transforming energy or motion, a compliant mechanism is a mechanical device that is capable of transforming energy

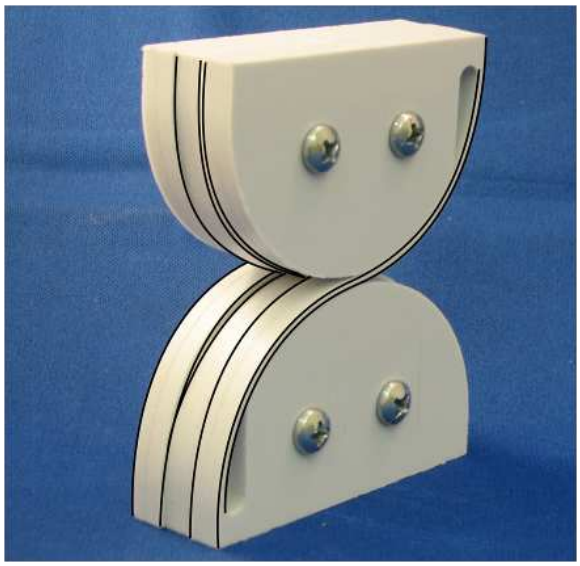

Figure 1.5: A compliant rolling-contact element.

or motion through the elastic deflection of one or more of its segments. The use of compliant mechanisms facilitates the production of devices that are precise [33, 34], small [35, 36], able to withstand harsh environments, and possess a specified force-deflection relationship [37, 38]. In recent years, advances have been made in the field of compliant mechanisms to mitigate many past challenges. Pseudo-rigid-body modeling [39], topology optimization [40–42], and finite-element analysis have made possible the design of large displacement compliant mechanisms capable of infinite life. Techniques such as inversion [43], isolation [43], and the use of contact-aided compliant mechanisms [44] have provided approaches for compliant mechanisms to withstand compressive loads without buckling. A better understanding of material science has allowed compliant mechanisms to be designed that reduce the effect that creep and stress relaxation have on compliant designs.

1.2.1 Compliant Rolling-Contact Elements

One class of compliant mechanisms uses flexures that conform to rolling bearing surfaces. Examples include compliant rolling-contact elements (CORE) [45–47], rolamite hinges [48, 49], Xr-joints [50], and cross-strip rolling pivots [51]. An example CORE joint is shown in Figure 1.5.

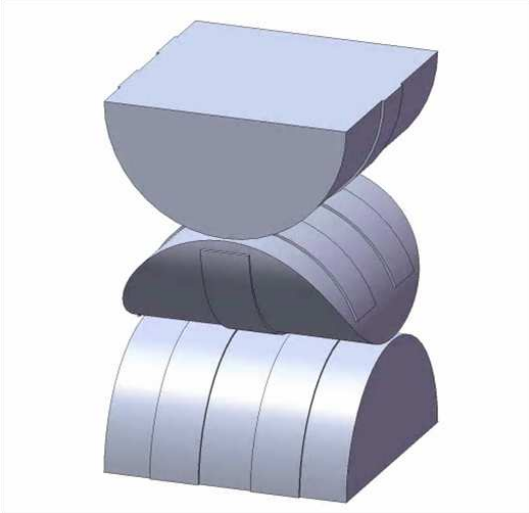

Figure 1.6: Biaxial Compliant Rolling-contact Element.

The CORE is assembled in such a manner that a flexible segment is placed between and attached to each surface. Such an assembly constrains the contacting surfaces to roll without sliding, virtually eliminating wear [48]. The mechanism can be constrained to maintain continuous contact by assembling multiple surfaces in an alternating fashion or by placing multiple flexures along the same surface, as shown in Figure 1.5. Further research has indicated that the force may be modified by changing the initial curvature of the CORE flexure, changing the curvature of the CORE surface, changing the cross sectional area of the flexure, changing the material properties, or by placing the flexures or a third member into tension [46, 47] [46, 47]. Jeanneau et al. [50] demonstrated that multiple mechanisms may be combined to provide multiple axes of rotation. An example of such a mechanism is shown in Figure 1.6. This class of compliant mechanism shows promise as the motion restoration component in a compliant artificial disc.

1.3 Current Technology for Spinal Implants

An ideal spinal implant will protect the spinal cord, bear load, restore the range of motion, restore the instantaneous axis of rotation, restore the kinetics, and provide a method of shock absorption/energy dissipation. There are several lumbar devices that attempt to restore some or all of these functions. These devices may be categorized as either spinal fixation systems or spinal

arthroplasty systems incorporating sliding bearings, traditional mechanical systems (springs, gears, cams, etc.) or elastomeric deformable centers.

1.3.1 Spinal Fusion

The first two requirements of an intervertebral disc, protection of the spinal cord and the ability to bear load, may be met through the use of spinal fixation systems. These systems use cages, plates, and other instruments to rigidly fix the superior and inferior vertebra of an FSU together. Often the IVD is removed and bone is allowed to grow into its place. Spinal fixation systems are the most common form of spinal instrumentation used in the United States. Proponents of this system indicate that a system of natural fusion, where the stiffness of the IVD increases with age, is common in older patients and may be the end state of the IVD [52]. However, evidence has indicated that fusion leads to an increased mechanical stress at the adjacent IVDs and may also accelerate disc degeneration at adjacent levels [53]. Furthermore, if enough spinal discs are fused the mobility of the patient is severely reduced.

1.3.2 Spinal Arthoplasty: Sliding Discs

Spinal arthroplasty devices incorporating sliding surfaces potentially provide the same benefits (i.e. protection of the spinal cord and ability to bear load) as spinal fixation systems with the added benefit of providing the patient with a range of motion similar to that of healthy discs. Although these discs provide the patient with enhanced flexibility, they have been indicated as a source of accelerated facet degeneration. This suggests that the instantaneous axis of rotation is not congruent with that of the natural disc and/or the facets are not being loaded to the same degree as they were when the IVD was healthy [54]. Furthermore, the sliding motion does not accurately reproduce the kinetics of the spine [55]. Spine arthroplasty devices were only recently introduced in the United States and long-term performance data is not yet available. While only a handful of cases of wear-induced osteolysis (resorption of the bone by the body) have been reported in spinal arthroplasty devices, the sliding friction-based functionality of these devices means that wear-induced osteolysis is still a concern [56]. Sliding disc spinal arthroplasty devices are the only type of spinal arthroplasty devices currently approved by the FDA for use in the U.S.

1.3.3 Spinal Arthoplasty: Elastomeric and Traditional Mechanisms Based Discs

An attempt to accurately reproduce the kinetics of the spinal disc has lead to the creation of two distinct classes of discs: those that use traditional mechanical systems and those that use an elastomeric center. Both classes of discs have exhibited advantages and disadvantages that have inspired and impeded their development. The mechanics behind discs based upon traditional mechanical systems are well understood but require multiple parts and assembly. These discs require sliding surfaces such as pin-joints or cams and produce wear [57, 58, 58]. Elastomeric discs, require a minimal number of parts, simplifying the implementation of the design. These discs flex in order to provide motion and do not have the same issues with wear debris. These discs also have the potential to provide some form of shock absorption/ energy dissipation. However, these discs are difficult to design, have issues with fatigue, have only shown limited ability to match the kinetics of the natural disc, and have demonstrated problems with bonding between polymer layers and the metal endplates used to secure the disc to the vertebra [59–61].

1.4 Approach and Document Organization

Previous work in the field of biomechanics has demonstrated the importance of proper biomechanics on implant design. To achieve the proper biomechanical response, several criteria must be met: (1) a designer must be able to properly analyze and model the response of the device, (2) the device must behave as expected, (3) the contribution of the surrounding tissue must be understood, and (4) the designer must be able to predict the response of the device in multiple individuals.

1.4.1 Contributions

This dissertation contributes to the field of compliant-mechanisms based implants by providing tools and techniques for the modeling and analysis of implants. Chapter 2 describes the modeling of a class of rolling contact elements. Specifically, this chapter discusses methods that may be used to vary the location and path of the axes of rotation as well as the force-deflection response. Chapter 3 demonstrates the validity of these models using benchtop testing. Additionally, a single level cadaveric test is used to demonstrate the prototypes behavior in the implanted

condition. Recognizing that there is a large intra and interpatient variation in the force-deflection response of the FSU, Chapter 4 adapts the pseudo-rigid-body model for use in the spine. This chapter demonstrates, through the use of a multilevel cadaveric test, the PRBM's ability to predict the global force-deflection response as well as adjacent-level effects due to changes (e.g. fusion, total disc replacement) at the operative level.

CHAPTER 2. MODELING AND DESIGN OF IMPLANT [1]

This chapter introduces the modeling and design of a Flexure-based, Bi-Axial, Contact-aided joint (FlexBAC). Additionally, this chapter demonstrates that these modeling techniques may be used to mimic the biomechanics of the human spine presented in the previous chapter.

2.1 Contact-Aided Compliant Spinal Discs

The FlexBAC is composed of two convex surfaces of varying curvatures. These surfaces may be a series of one or more circular, elliptical, or flat segments. A simplified version consisting of flat endplates and a circular center is shown in Figure 2.1. The curvature and length of the surface may vary in order to obtain the desired resistance to force, range of motion, location of the instantaneous axis of rotation, and kinetics. The device's center is connected via one or more flexures as to constrain the device to roll. The endplates to which the center is connected may also contain multiple circular, elliptical, or flat segments. An embodiment of the mechanism is illustrated in Figure 2.2.

[1] Portions of this chapter have been published in [1]

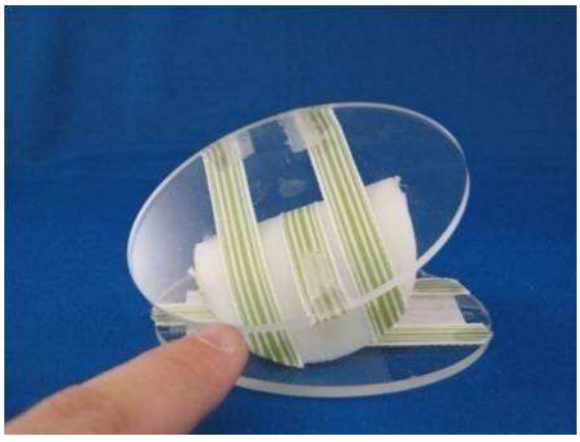

Figure 2.1: Simplified FlexBAC disc showing location and orientation of flexures.

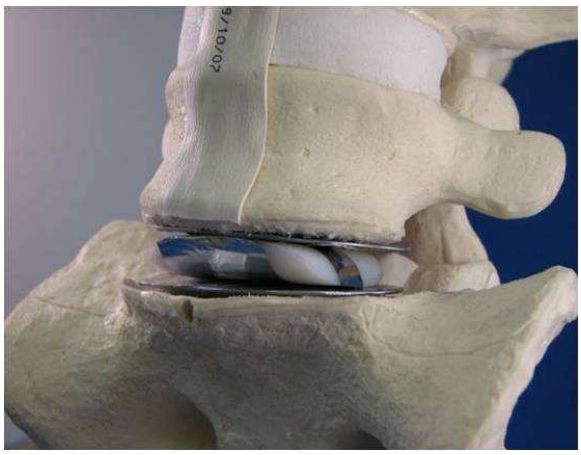

Figure 2.2: Prototype FlexBAC inserted into the disc space of a spinal model.

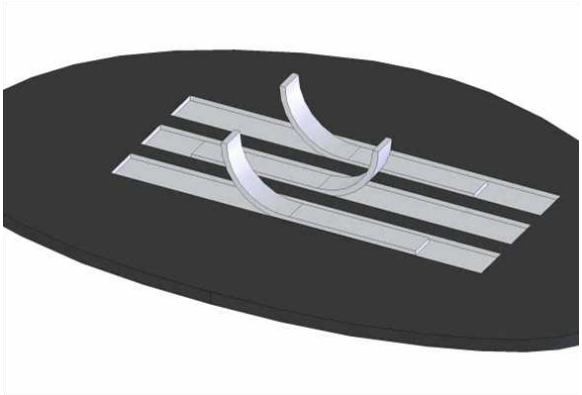

Figure 2.3: Endplate demonstrating the principle of recessed bands.

2.1.1 Forces

The FlexBAC's structure is well suited for the large compressive forces that exist in the spine (Table 1.1). The compressive load is readily transferred through the center component. The compressive load has little effect on the flexures due to its orientation with respect to the flexures. What effect the compressive load has on the flexures may be minimized by recessing the flexures into the endplate, similar to the method shown in Figure 2.3. This transfers the compressive force through the curved surface and directly into the endplate. Constructing the mechanism in this manner mitigates the direct compression that the flexures experience. The same effect may be achieved by recessing the bands into the rolling center. The stress in the flexures for the case of

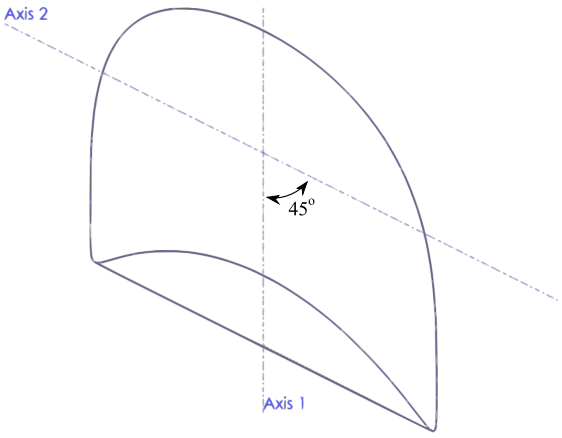

Figure 2.4: Isometric view of the FlexBAC whose 2nd axis of rotation is coupled 1:1 with the direction of the primary axis of rotation.

uni-axial movement is calculated as

$$\sigma = \frac{F_C \sin(\theta)}{A} + \frac{Eh}{2R_s} - \frac{Eh}{2R_o} \tag{2.1}$$

where R_o and R_s are the initial radius of curvature for the flexure and the radius of curvature for the constraining surface, respectively. F_c is the compressive force exerted on the disc space. A and h are the cross-sectional area and the height of flexure. θ is the angle of flexion-extension or lateral bending. The relationship between the distance along the flexure, x, and the angle of flexion-extension, θ, is

$$x = R_s \theta \tag{2.2}$$

2.1.2 Kinematics

The kinematics of a FlexBAC artificial spinal disc depends on the selected curvature arc lengths and radii, as well as the axis of orientation. The upper and lower surfaces may be manufactured such that the axes of rotation are perpendicular, as shown in Figure 2.1, or the axis may be oriented to exhibit coupled motion (i.e. non-perpendicular axis of rotation), as shown in Figure 2.4.

For the case of the center surface rolling without slip on a flat endplate, the maximum range of motion the mechanism provides is the same as the central angle of the surface (ratio of arc length

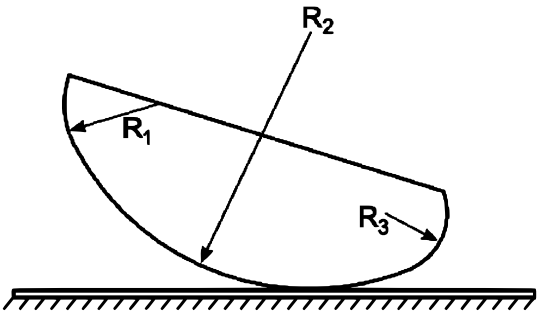

Figure 2.5: Rolling-contact surface containing multiple curvatures.

to radius of curvature). When the center rolls on a curved endplate the relationship between the central angle of the center surface, $\theta_{surface}$, and the maximum range of motion, $\theta_{\max}$, is

$$\theta_{\max} = \left(1 + \frac{R_{surface}}{R_{endplate}}\right) \theta_{surface} \tag{2.3}$$

where $R_{surface}$ and $R_{endplate}$ are the radius of curvature of the surface and endplate respectively. As the mechanism rolls without slip, the location of the centrode is on the contact surface. A continuous centrode (locus of instantaneous centers) may be created by a single surface or by joining two or more curvatures together, as shown in Figure 2.5. A non-continuous centrode may be created by allowing two flat surfaces to come in contact with each other, as shown in Figure 2.6.

For small angle deflections, the instantaneous axis of rotation should lie on or near the centrode. This is verified graphically by forming two construction lines between two points on the endplate at maximum extension and two points on the endplate at maximum flexion. Perpendicular bisectors of the construction lines are then formed. The instantaneous axis of rotation is the intersection of the perpendicular bisectors. This process and the location of the instantaneous axis of rotation in flexion-extension and lateral bending are shown in Figure 2.7. Using this information, the surface can be designed to mimic the kinematics of the natural disc.

2.1.3 Kinetics

The kinetics of the FlexBAC can be modified through one or a combination of the six methods used to modify the force-deflection characteristics of the CORE :

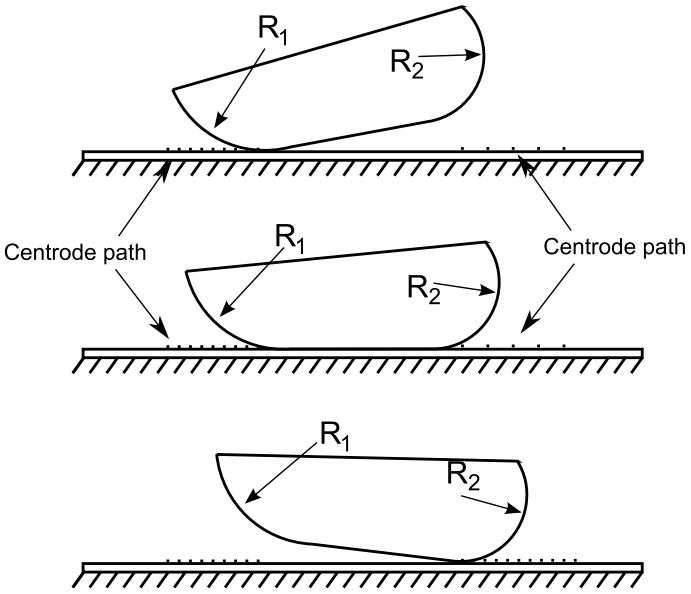

Figure 2.6: Rolling contact surface demonstrating non-continuous centrode.

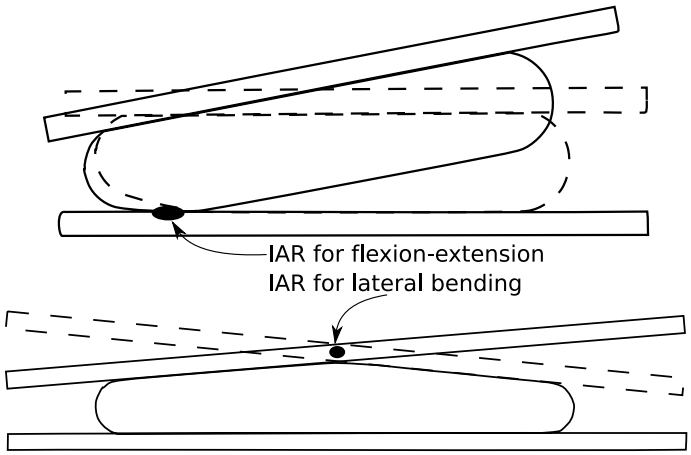

Figure 2.7: The instantaneous axes of rotation of the FlexBAC in flexion-extension (top) and lateral bending (bottom).

- change the initial curvature of the flexure
- change the curvature of the surface
- change the cross-sectional area of the flexure
- change the material properties
- place the flexures into tension

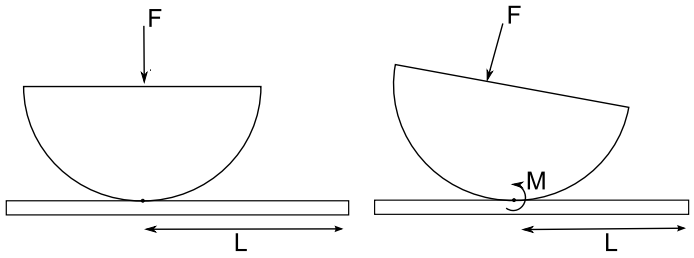

Figure 2.8: When the compressive forces act on the spine through the instantaneous axis of rotation (left), no moment will be generated. When the forces act in direction that is not through the instantaneous axis of rotation, a restorative moment will be generated.

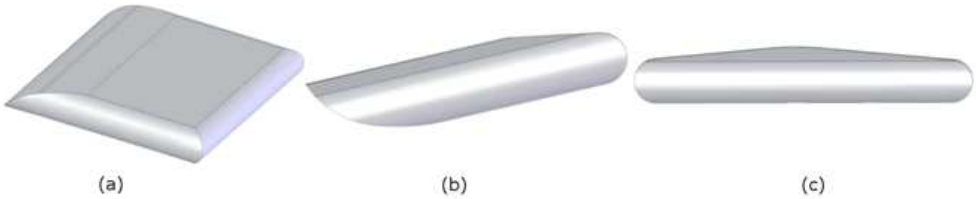

Figure 2.9: Surface geometry of the FlexBAC.

- place a third member into tension

An additional method to generate the desired force deflection relationship is through the use of geometry and the compressive nature of the spine. The compressive preload inherit in the spine has the ability to either aid or hinder the restoration of the disc, as illustrated in Figure 2.8. As the mechanism is displaced, the location of the instantaneous axis of rotation, L, changes. As a result, the compressive load (Table 1.1) no longer passes through the instantaneous axis of rotation and a restoring moment is generated.

2.1.4 Embodiment of a FlexBAC Disc

The rolling surface of the Flexure-based Bi-Axial Contact-aided (FlexBAC) artificial disc that satisfies the biomechanical requirements of sections 1.1.1-1.1.3 is shown in Figure 2.9. The disc is composed of two main curvatures where the motion occurs (R = 100 mm flexion-extension and 30 mm lateral-bending). The axes of these curves lie perpendicular to each other and the location of the instantaneous axis of rotation is shown in Figure 2.10.

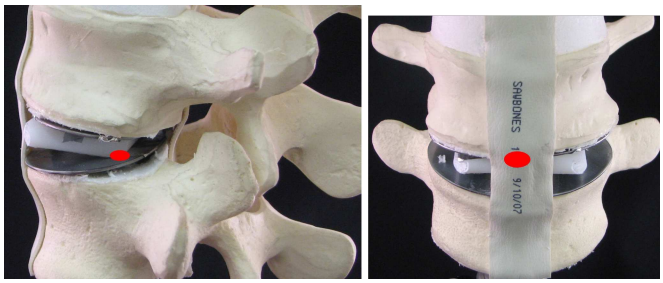

Figure 2.10: Location of the instantaneous axes of rotation for flexion-extension and lateral bending.

The range of the mechanism shown in Figure 2.9 was designed to be 4 degrees extension, 7 degrees flexion, and 4 degrees lateral bending in both the left and right directions. The axial rotation (maximum one sided rotation of 1.5 degrees) is sufficiently small that it is expected to be allowed for by the torsional compliance of the system, as is common with some spinal fixation systems [31].

Although the force-deflection relationship of the FSU is shown in Figure 1.3, the specific contribution of the disc to this force-deflection relationship is still a topic of study. As the force deflection characteristic of the natural disc and the location of the compressive load become better understood as the result of ongoing studies, one or a combination of the methods outlined in section 2.1.3 should be able to provide the proper force-deflection characteristic.

To demonstrate this ability, the force-deflection response of the entire FSU in flexion-extension was matched using a change in initial curvature of the flexure. The equation for the force-deflection curve for flexion-extension was determined by a sum of least squares method.

$$M = 0.922\theta - 0.0375\theta^2 + 0.046\theta^3 - 0.020\theta^4 + 0.0023\theta^5 \tag{2.4}$$

where M is the restorative moment at some position θ. Neglecting the compressive load, the initial radius of curvature of the flexure, R_o, needed to generate a specified moment, M, when constrained to an upper, R_u, and lower, R_l, surface may be calculated using the Bernoulli-Euler principle

$$M = EI(\frac{1}{R_u} + \frac{1}{R_l} - \frac{2}{R_o}) \tag{2.5}$$

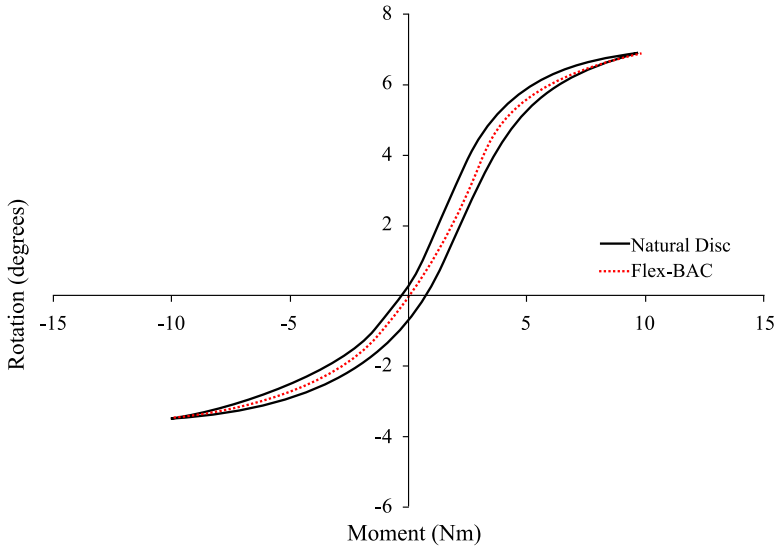

Figure 2.11: Force-deflection characteristics of the FlexBAC and the natural disc in flexion-extension.

Equations (1) to (3) may be used to calculate the change in the initial radius of curvature needed. Using the material properties of PEEK-OPTIMA(CF) (flexural modulus and strength 15 GPa, and 288 MPa respectively) and Titanium 6Al-4V (flexural modulus and strength 105 GPa, and 795 MPa respectively), the geometry outlined above, and assuming a total flexure width of 40 mm (20 mm wrapped in each direction) an optimization problem was established to minimize the maximum stress in the flexures, while producing the desired moment. The optimization routine was subject to the constraints of a constant surface radius, $R_l = 100mm$, endplate radius, $R_u = \infty$, and flexure thickness and width. The design variables were initial radius of curvature, and thickness of the flexure. The optimum flexure thickness for PEEK and titanium were calculated to be 2.4 mm and 1.27 mm respectively. The Force-deflection relationship compared to the natural disc is shown in Figure 2.11. The relationship between rotation and maximum stress for PEEK and titanium flexures are shown in Figure 2.12.

2.2 Conclusions

The biomechanics of the human spine are fundamentally different than those of diarthrodial joints. As a result, the design of an artificial spinal disc requires a departure from the sliding surface designs used in other total joint arthroplasty designs. The Flexure-based Bi-Axial Contact-aided

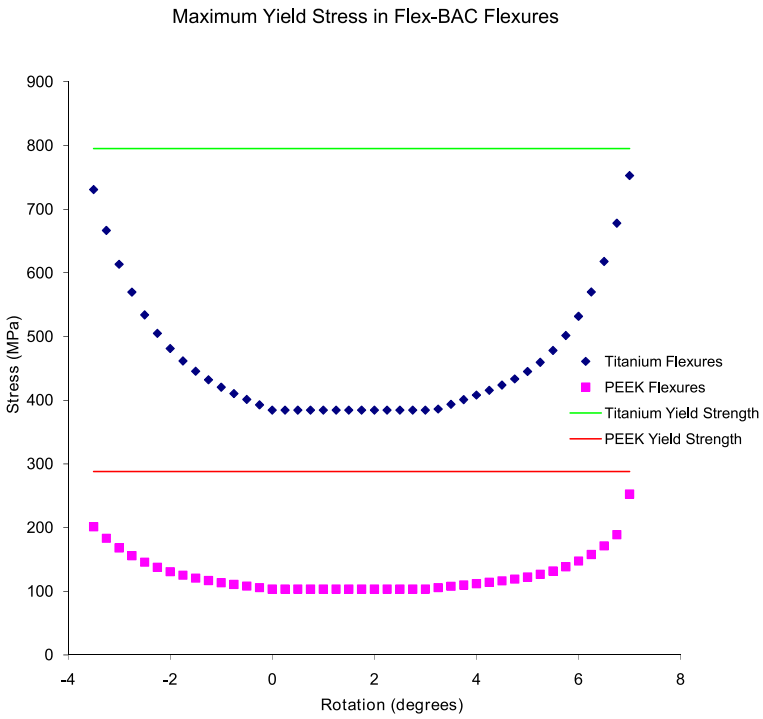

Figure 2.12: The maximum stress for PEEK and titanium flexures in relation to angle for flexion-extension.

disc presented in this chapter offers another alternative to artificial spinal discs. This alternative has the potential to mimic the biomechanics of the natural disc in terms of load-bearing properties, range of motion in flexion-extension and lateral bending, the location of the instantaneous axis of rotation, and the kinetics. Contact-aided compliant mechanisms and compliant mechanisms in general also have the potential to virtually eliminate wear, dramatically reducing the potential for implant loosening through osteolysis.

CHAPTER 3. MODEL IMPLEMENTATION AND VERIFICATION [1]

The previous chapter introduced various techniques to modify the quality of motion of a contact-aided compliant mechanism and demonstrated its use in the creation of a physiological instantaneous axis of rotation (IAR). While the use of a single location for the IAR is the current practice, it may not reflect proper biomechanics. In a healthy functional spinal unit the location of the IAR is known to vary. This chapter expands on the use of contact-aided compliant mechanisms as spinal arthroplasty devices by focusing on the Quality of Motion (QOM), including the helical axes of motion, of the functional spinal unit. Additionally, the device developed in this chapter incorporates the compressive force on the intervertebral disc space in the device design.

3.1 Introduction

Recent studies indicate that the long-term success of spinal instrumentation, including total disc replacements (TDRs), depends strongly on biomechanics. Multiple studies have shown that the altered biomechanics of spinal fusion increase stress within the intervertebral disc (IVD), facets, and ligaments of adjacent segments [62–64]. These altered biomechanics may lead to poor long-term clinical results that require reoperation. The current generation of TDRs seek to restore one aspect of biomechanics: the quantity (i.e. range) of motion. As a result, short-term data indicates, when compared to spinal fusion these TDRs provide a shorter recovery time, lower cost, and increased patient satisfaction [65, 66].

However, the lack of quality of motion (defined as the replication of appropriate helical axes of motion [HAM] and moment-rotation response) of the current generation of TDRs may lead to less-than-ideal long-term clinical outcomes, such as facet degeneration and adjacent segment disease [67–69]. Misalignment of the HAMs between the TDR and the functional spinal unit (FSU) may limit mobility and load-sharing of the FSU [70, 71, 71] and the load-sharing of adjacent

[1] Portions of this chapter are currently in review for publication in *Spine*

segments [72]. As a result, the mobility of the current generation of TDRs are highly dependent upon proper placement. Additionally, unlike the hip or knee, where the moment-rotation response of the joint is determined by the surrounding tissue, the cartilaginous IVD has an intrinsic nonlinear moment-rotation response [21]. Failure to match this response may cause the implant to exhibit a slip-stick motion [55] as well as increase stress and/or induce remodeling in adjacent segments [73].

The current generation of sliding-bearing-surface disc replacements cannot provide for the same intrinsic quality of motion (QOM) and energy storage that the natural IVD provides. As a result, current disc replacements must rely on the surrounding tissue or additional elastic elements, such as springs, to provide QOM. Discs that rely on the surrounding tissue often exhibit a stick-slip movement [55] that imposes additional loads on the facets [74] and surrounding segments and may lead to accelerated degeneration [67], while discs that rely on additional elements, such as springs, may become overly complex.

The embodiment required to achieve natural QOM may be simplified through the use of compliant mechanisms. Compliant mechanisms are devices that receive motion through the deflection of one or more members [39]. By combining structural and elastic elements, compliant mechanisms have shown several advantages over traditional rigid-body mechanisms. These advantages include a reduced number of parts [75], resistance to harsh or corrosive environments [39], higher precision [34, 76, 77], wear-free motion [39], ease of miniaturization [78, 79], and tailorable force-deflection responses and axes of rotation [39].

Due to the significant effect that biomechanics have on long-term outcomes, QOM considerations should be incorporated into the design phase of the implant. These design considerations should include the proper moment-rotation response (Figure 3.1(a)) and proper HAM (Figure 3.1(b)). It is also important to consider implant durability (e.g. wear, fatigue, and creep) and surgical robustness in the early stages of design. As a result of these requirements and the advantages of compliant mechanisms, compliant mechanisms may offer appealing characteristics when applied to the design and development of total disc replacements.

This work outlines the development, validation, and testing of a compliant mechanism based TDR developed at Brigham Young University (Provo, UT) and licensed to Crocker Spinal Technologies (Park City, Utah) under the tradename FlexBAC™ (Figure 3.2), which was designed

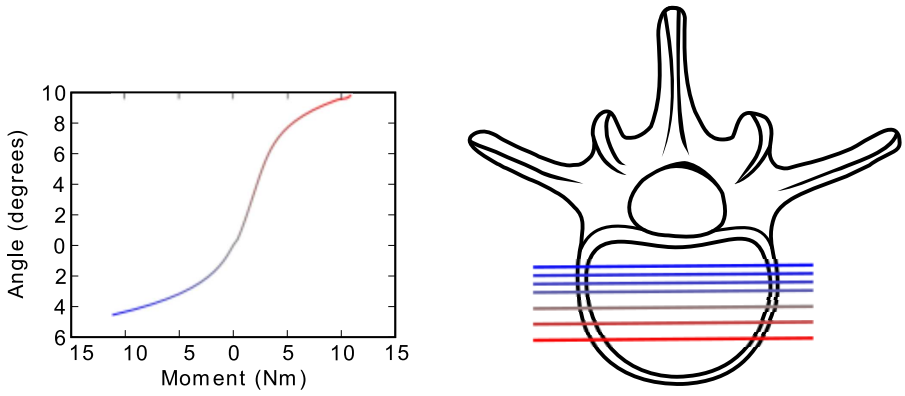

(a) (b)

Figure 3.1: (a) Median moment-rotation response and (b) HAM of the lumbar spine [71] in flexion-extension. The HAM of motion in (b) are represented by lines, the shading of which corresponds to the angular response in (a).

Figure 3.2: The prototype total disc replacement.

to specifically match the segmental biomechanics of the healthy lumbar spine. The primary hypothesis of this study is that the biomechanical behavior of the implanted spine could be designed and predicted prior to cadaveric implantation using traditional design methods coupled with biomechanical analysis techniques.

3.2 Methods and Materials

A three-step process was used for the design and testing of the implant: (1) a specific QOM profile was selected and designated as the target functional specification, (2) nonlinear optimization was used to determine the geometry and mechanical response of the implant and to match the selected QOM profile, (3) bench-top and cadaveric testing were used to verify the QOM performance of the implant.

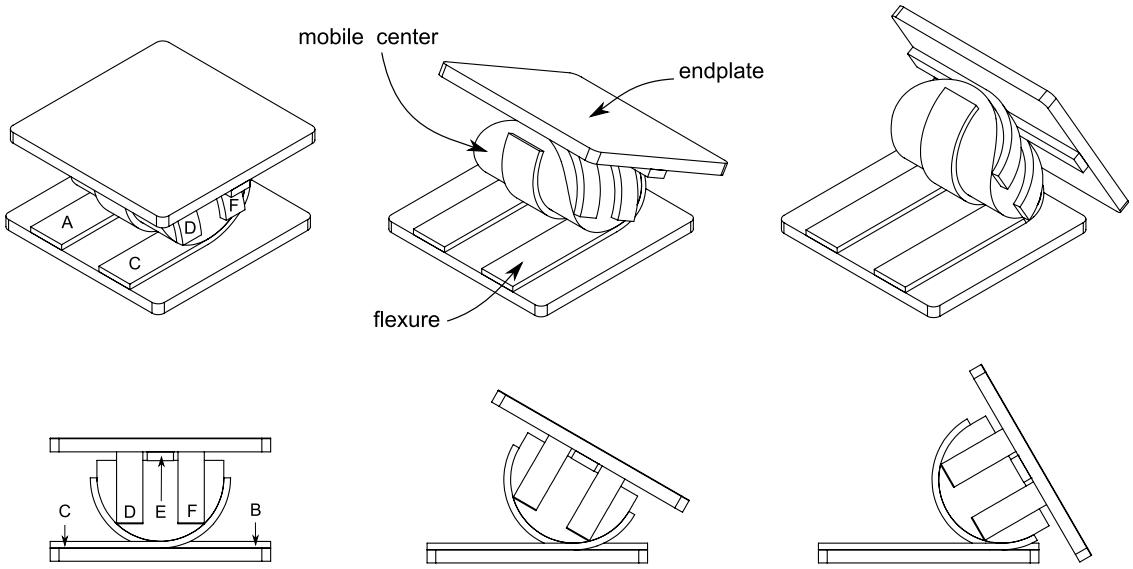

Figure 3.3: The implant motion profile as viewed from an isometric view (top) and sagittal view (bottom) for an idealized geometry.

3.2.1 Device Design

A description of the mathematical modeling of the device is given in Chapter 2 and an example of the analysis in Appendix A, but a brief description of the device is given here for completeness. The device, shown with idealized geometry in Figure 3.3, consists of multiple flexures (labeled A-F in Figure 3.3), a mobile center, and superior and inferior endplates. Motion in the device is generated through elastic deformation of the flexures (Figure 3.3), making it a compliant mechanism. As the device is displaced, the flexures are transferred from one surface to another, creating a rolling motion [45, 50]. Because the mechanism rolls without slip, wear is not generated from articulating surfaces. Figure 3.3 shows a generic geometry with constant radius, but the quality and quantity of motion of the mechanism may be modified by changing the geometry of the mobile center and flexures [46, 80].

A nonlinear optimization routine was used to match a specific QOM profile. The target QOM profile was created from the median moment-rotation response of 10 available profiles. Due to the large stochastic errors related to the measurement of the finite HAM [28], the location and path of the HAM were selected such that the HAM were consistent with those reported in [28, 71].

Once the specific target QOM profile was selected, a numerical model was combined with nonlinear optimization to design a device that matched the profile. Mathematical models were

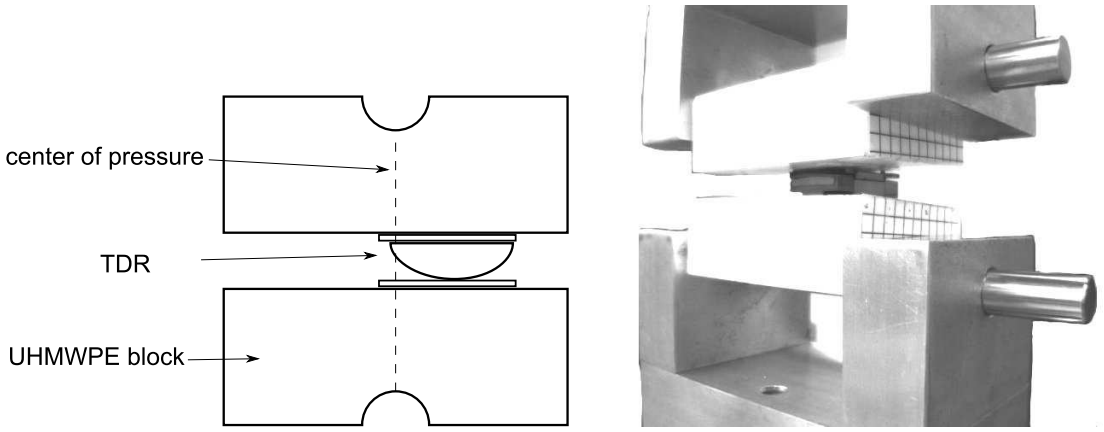

(a) (b)

Figure 3.4: (a) Functional schematic of modified F1717, with center of pressure illustrated by dotted line, and (b) actual test setup.

used to determine the stress, HAMs, and force-rotation response of the device [39, 80]. A nonlinear gradient-based optimization routine was used to optimize for the correct surface and flexure geometry that related to the desired performance. The optimization routine was constrained such that the device would (1) have an infinite fatigue life under coupled loading conditions of $\pm$10Nm in flexion-extension, lateral bending, and axial rotation; (2) would fit in an implant space with dimensions no greater than 22, 36, and 12 mm in the anterior-posterior, left-right, and superior-inferior directions, respectively; and (3) match the selected QOM profile in flexion-extension and lateral bending.

3.2.2 Isolated Implant Testing

The force-rotation response of the implant was initially verified through a modified F1717 [81]. The prototype was placed between two ultra high molecular weight polyethylene (UHMWPE) blocks fixed to a tensile/compressive tester through pinned connections. The implant was oriented in order to place the center of pressure 4 mm from the anterior endplate edge (see Figure 3.4). The UHMWPE blocks were then compressed axially and the angle of rotation determined through optical markers located on the UHMWPE blocks. These results were compared to the values predicted during the design phase.

3.2.3 Integrated Implant Testing Setup

A single-level cadaveric test was used to verify that the designed-for implant behaved as expected in vitro.

Test Specimen

The cadaveric fresh-frozen specimen (L3-L4, female, age 65) was acquired from an accredited tissue bank under the approval of an internal review board. The specimen was carefully dissected to preserve the ligaments and disc. The superior and inferior vertebral bodies were potted into polyester resin and optical markers were attached to facilitate motion tracking during testings.

Spine Tester and Testing Conditions

The specimen was tested in the spine tester shown in Figure 3.5 and based on [82]. A pure moment load was applied using a stepper motor. The motor was micro-stepped to a step resolution of 0.09° per step and coupled to the superior potting fixture through two universal joints and a ball spline. (This configuration allows the specimen to be driven in one axis of motion while permitting coupled motions.) The specimen was then rotated 90° and tested in lateral bending. Axial rotation was tested by moving the motor to the top of the machine. All axes of motion were tested at a rate of $1\frac{deg}{sec}$ and under a compressive follower-load [83] of 440 N. An environmental chamber permitted the specimen to be tested at 32 $^\circ$C and $>$ 95% humidity. Camera calibration was performed within the chamber to account for optical aberration from the environmental chamber. Rotation of the vertebral bodies was determined through optical markers [84].

3.3 Results

The method yielded an implant that met the design requirements. The theoretical QOM profile in flexion-extension and lateral bending matched the designed-for QOM profile. The Von-Mises mean and alternating stress of the device predicts that the design is capable of an infinite fatigue life under coupled loading conditions of $\pm$10Nm. The resulting prototype device, including

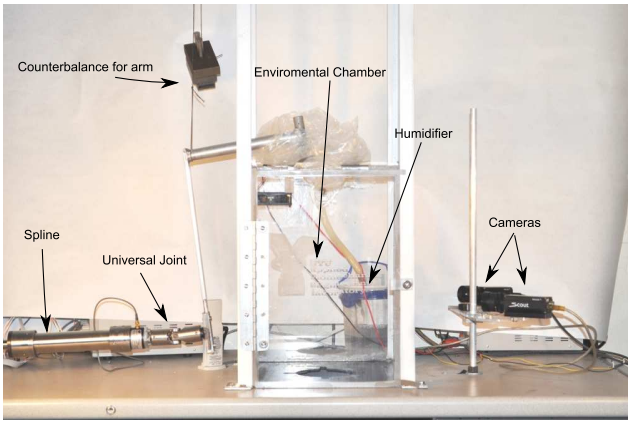

Figure 3.5: Spine tester and environmental chamber.

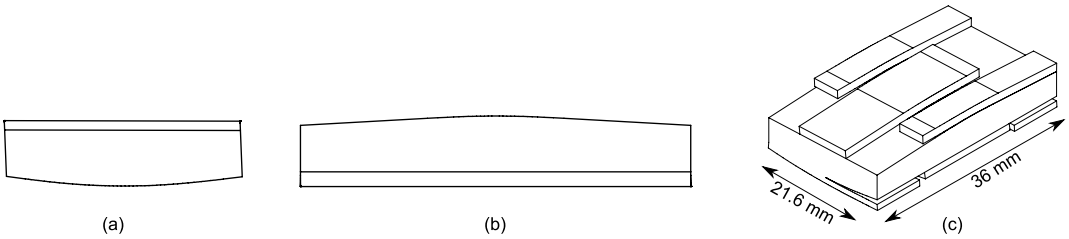

Figure 3.6: Resultant prototype surface geometry without flexures or endplates, in the (a) sagittal and (b) frontal planes. (c) An isometric view of the prototype surface and flexure geometry without endplates A photograph of the prototype with endplates is shown in Figure 2.

endplates, measures 21.6 mm, 36 mm, and 11 mm in the anterior-posterior, left-right, and superior-inferior directions, respectively, and is shown in Figures 3.2 and 3.6.

The isolated testing showed agreement between the predicted and measured states as shown in Figure 3.7. The measured results show that the device demonstrates a nonlinear stiffness throughout the motion of the device. The correspondence of the nonlinear stiffness may also be seen in Figure 3.7.

The range of motion of the integrated and [intact] FSU were 8.6° [9.3°] flexion, 4.3° [3.3°] extension, 3.75° [4°] left-lateral bending, 7.8° [5°] right-lateral bending, 2° [2.75°] right-axial rotation, and 1.75° [3.25°] left-axial rotation. The moment-rotation response of the implant, when integrated into the FSU, and the moment-rotation response of the intact FSU in flexion, extension, and lateral bending, are shown in Figure 3.8(a) and Figure 3.8(b). The QOM in flexion-extension was compared to the designed-for case and is shown in Figure 3.9(a). The consequences of non-

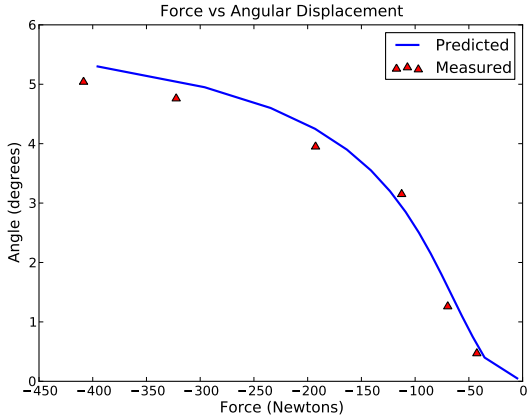

Figure 3.7: The force-rotation response in isolated testing conditions as compared to the predicted values.

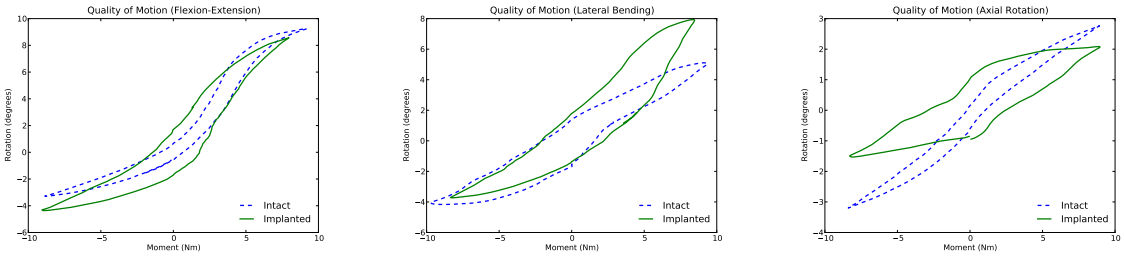

(a) (b) (c)

Figure 3.8: The moment-rotation response of the FSU before and after implantation, shown in (a) flexion-extension, (b) lateral bending, and (c) axial rotation.

ideal surgical misplacement on the QOM of the implant by ± 4 mm was also calculated and is shown in Figure 3.9(b).

3.4 Discussion

As demonstrated in Figure 3.8, the QOM of the implanted and intact FSUs in flexion-extension and lateral bending were similar. The small deviation for left-lateral bending, shown in Figure 3.8(b), can be attributed to elastic deformation of the artificial endplate. This deviation was caused from a Y-shaped endplate design that resulted in the left side of the endplate being substantially less stiff than the right side. The Y-shaped endplate was not explicitly included into

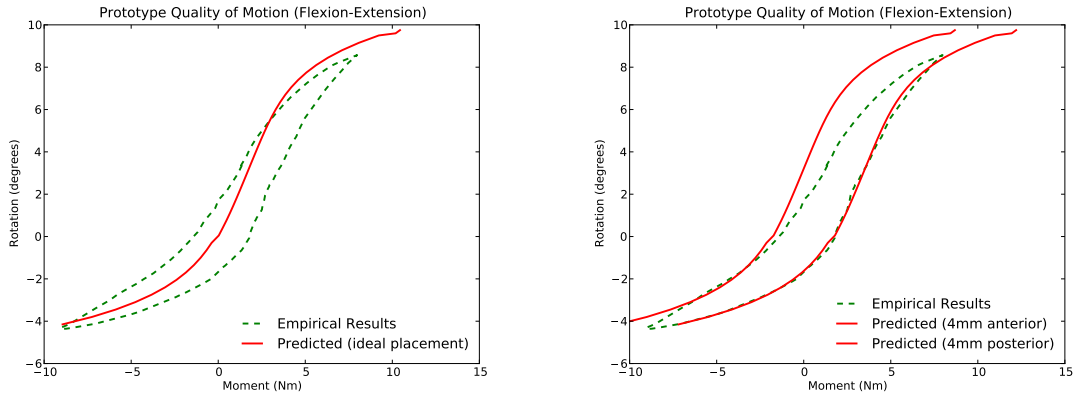

(a) (b)

Figure 3.9: The measured response of the integrated FSU and (a) the predicted QOM when placed in its proper location and (b) the predicted QOM when misplaced by ± 4 mm to its ideal location.

the design process. The endplate design has since been modified to be symmetrical about the sagittal plane.

The ability of the implant to replicate complex spinal biomechanics has significant long-term clinical implications. The implant was able to prevent the stick-slip motion associated with the current generation of implants by providing a resistance to motion. Additionally, since the stiffness of the FSU with the implant was equivalent to intact stiffness, one would expect similar motion patterns to the intact condition. Whereas the current generation of TDRs produce hypermobility for some movements, and hypomobility for others, the implant under consideration would produce consistent motion patterns. Because both hyper- and hypo-mobility have both been attributed to the degeneration of the spine [73], consistent motion patterns become crucial for the long-term maintenance of spinal health.

Perhaps of most importance, the QOM of the implant as measured through bench-top and in-vitro testing behaves as predicted. The ability to predict and design for specific QOM profiles prior to cadaveric testing allows for rapid design iterations, as well as predictable biomechanics. This process opens the door to the possibility of patient-, gender-, or age-specific implants. Specific implants for specific QOM profiles would allow for the large variation in QOM profiles across the degenerative cascade [85].

Compliant mechanism-based design is not without its own set of challenges. One of the greatest challenges is that compliant mechanisms provide motion through deflection, which cou-

ples motion with stress. Careful consideration must be given to the selection of both material and design characteristics to prevent fatigue failure. This selection criterion can make the design process much more difficult than traditional rigid-body mechanics because one must also account for coupled motions that produce bi- or tri-axial stress states. Fortunately, there exists a wide range of materials (such as titanium, peek, and silicone) that exhibit properties that make them well suited for biologically-compatible compliant mechanisms. Some (e.g. titanium) exhibit well-known fatigue and creep characteristics that, when used with compliant mechanism design techniques [39], can provide for an implant capable of an infinite fatigue life such as the implant studied here. The compliant nature of the implant also indicates that motion-induced wear may be eliminated [39]. Additional testing is needed to confirm this.

3.5 Conclusion

Incorporation of compliant mechanism design theory into the foundational stages of the design process resulted in a TDR design that holds high potential for decreasing degeneration of the adjacent segments and the operative level facets. Due to the compliant nature of the implant, motion-induced wear is not anticipated. The results show a high fidelity between the predicted quality of motion and the measured quality of motion. Additionally, the implant, when integrated into the FSU, was able to successfully mimic both the range of motion and the segmental QOM of the intact FSU. As a result of the close approximation of the implant to the intact condition, one would expect minimal changes to the biomechanics of the segments adjacent to the operative segment. Although the potential to mimic the QOM of the FSU is promising, additional preclinical research is needed to determine the appropriate QOM profile(s) for the population at large.

CHAPTER 4. PSEUDO-RIGID-BODY MODEL [1]

The previous chapters demonstrated the use of contact-aided compliant mechanisms to mimic specific QOM profiles. As large intra and interpatient variation in QOM profiles exist, it is important to consider the effects that these variations may have on motion at adjacent segments. This chapter introduces and demonstrates the use of the pseudo-rigid-body model in predicting adjacent-level effects.

4.1 Background

The functional spinal unit (FSU) responds to changes in its mechanical environment. Like bone [86], the intervertebral disc (IVD) exhibits a "lazy zone" or "safe-window" of mechanical stimulus in which remodeling does not occur [73]. A similar "safe-window" has been shown to exist in synovial joints, such as the facets [87]. As remodeling may occur outside of the "safe-window", it is important to understand the consequences of changes to spinal biomechanics.

Due to the compliant nature of the spine, the stress within the IVD and facet joints is coupled with its motion. Hypermobility of the FSU increases stress in the FSU and can greatly accelerate the degeneration of IVDs and facets [73]. As hypermobility is commonly exhibited in segments adjacent to spinal fusion, it has been implicated as a factor in adjacent segment disease [53].

Although less studied, it has been shown that hypomobility can also lead to degeneration of IVDs and facets [73, 87]. Hypomobility has been implicated in degeneration of the articular surface and osteophyte formation of the facet joints [87]. Furthermore, hypomobility decreases the mechanical stimulus for tissue repair, leading to a higher probability of degeneration when overload is experienced [73].

[1] Portions of this chapter are currently in review for publication in *Clinical Biomechanics*

Fusion, total disc replacements (TDRs), and posterior dynamic stabilization systems can have adverse effects, such as hyper- and hypomobility, on spinal biomechanics. As both hyper- and hypomobility may lead to degeneration, predicting the effects that various changes to the mechanical properties of the FSU have on the operative/injured level as well as on adjacent levels is valuable. Understanding these effects can be particularly useful in creating procedures and implants that minimize these effects. Three modeling techniques are currently employed to analyze adjacent level effects: animal models, finite element analysis (FEA), and cadaveric testing.

Animal models, when appropriately implemented, have the ability to predict biological changes to surrounding tissue with a high degree of fidelity. Additional instrumentation may be used to examine the mechanical stress at critical locations. However, due to the upright nature of human posture, a suitable animal model of the human spine has not yet been identified [88].

FEA, another common technique [89], provides the ability to model deformations and stress at every level throughout the FSU [90, 91]. As a result, FEA provides excellent insight into adjacent level effects. However, the time and cost of producing and validating an FEA model often limits the number of specimens and/or levels that can be examined in a cost-effective manner. Other techniques, such as simplified FEA beam models [92] and spring and pin-joint models [93], have also been used to investigate various aspects of spinal biomechanics such as sagittal alignment and muscle reaction forces.

Cadaveric testing enables the in-vitro examination of the effects of mechanical changes on adjacent levels. However, the nature of cadaveric testing often means that there is a disproportionate number of spines where degeneration due to age has already degraded the mechanical properties. Additionally, the cost of cadaveric testing often makes it prohibitive in the early stages of implant design.

While each of the current methods has its advantages and limitations, a model capable of predicting adjacent level effects in a quick, accurate, and cost effective manner would be a valuable tool. Such a model may be particularly beneficial in early stage development of new processes and implants, before prototypes exist for testing and while design changes are easily made. Similar modeling needs are found in the field of compliant mechanisms.

Compliant mechanisms are mechanisms that achieve their motion through elastic deformation. The IVD is a naturally occurring compliant mechanism. It is therefore reasonable to

consider compliant mechanism analysis methods for use in the study of spinal biomechanics. The Pseudo-Rigid-Body Model (PRBM) is a well established, accurate, and efficient method of modeling compliant mechanisms [39, 94, 95]. The PRBM gains its efficiency by approximating elastic elements as appropriately sized rigid links, pin joints, and springs. Rigid-body kinematics and kinetics may be used with the resulting PRBM to analyze the system.

The aim of this study is to demonstrate the use of the PRBM in the prediction of adjacent level effects. The primary hypothesis is that the PRBM can accurately predict the global stiffness of a multilevel spine and the contribution of each individual level. Additionally, it is hypothesized that the PRBM can predict the effects that changes on one level have on adjacent levels.

4.2 Methods

4.2.1 Pseudo-Rigid-Body-Model

A PRBM of the lumbar spine (L3-S1) was created with each vertebral body of the FSU approximated as a rigid-body link. The rigid-body linkages were then connected to superior and inferior linkages by pin-joints at the location of the respective instantaneous axes of rotations (IAR), as illustrated in Figure 4.1. Nonlinear springs (k_1, k_2, and k_3) were used to approximate the nonlinear stiffness of each FSU. The stiffness of the springs were determined through differentiation, as a function of local angular displacement (θ_1,θ_2,θ_3,) of the non-linear force-deflection curve of the entire FSU under a compressive follower load [83, 96].

Using the model shown in Figure 4.1, the location of L3 may be expressed in complex form as $R_0e^{i\theta_0} + R_1e^{i\theta_1} + R_2e^{i\theta_2} + R_3e^{i\theta_3}$. If it is assumed that the follower load eyelet is attached to a rigid-body link at a relative distance of a. The load-path of the follower load is calculated as

$$\theta_{LP_{01}} = \arctan\left(\frac{R_1 a_1 \sin(\theta_1)}{R_0 + R_1 a_1 \cos(\theta_1)}\right) \tag{4.1}$$

$$\theta_{LP_{12}} = \arctan\left(\frac{(1-a_1)R_1 \sin(\theta_1) + a_2 R_2 \sin(\theta_2)}{(1-a_1)R_1 \cos(\theta_1) + a_2 R_2 \cos(\theta_2)}\right) \tag{4.2}$$

$$\theta_{LP_{23}} = \arctan\left(\frac{(1-a_2)R_2 \sin(\theta_2) + a_3 R_3 \sin(\theta_3)}{(1-a_2)R_2 \cos(\theta_2) + a_3 R_3 \cos(\theta_3)}\right) \tag{4.3}$$

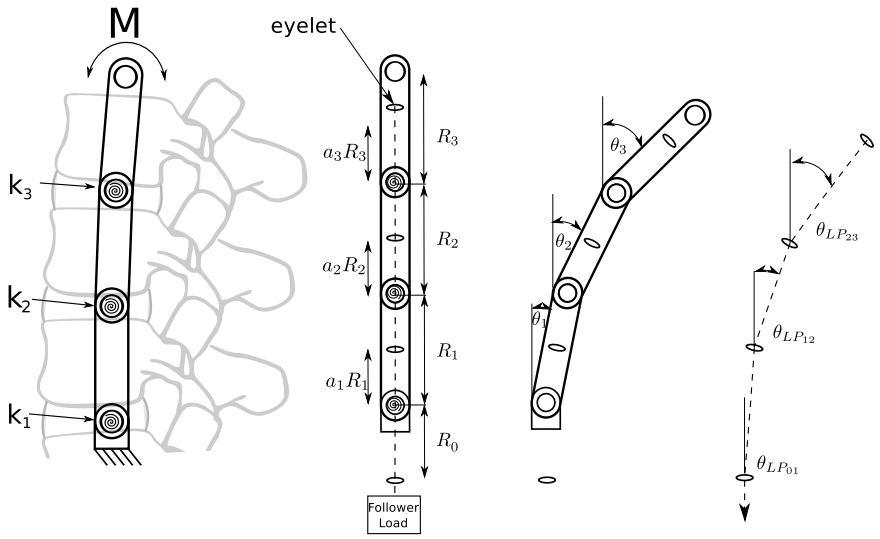

Figure 4.1: The PRBM and its nomenclature for flexion-extension.

for L5-S1, L4-L5, and L3-L4, respectively, R_1, R_2, and R_3 are the rigid-body lengths of the PRBM and θ_1, θ_2, θ_3 are the angular position of the vertebral bodies as measured from the upright vertical. The distance R_0 is the vertical distance to the lower potting fixture eyelet.

A free-body diagram is then used to determine the contribution of the load path on the reaction force (F_x and F_y) at the eyelet,

$$F_x = F_L(\cos(\theta_{LP_{Sup}}) - \cos(\theta_{LP_{inf}})) \tag{4.4}$$

$$F_y = F_L(\sin(\theta_{LP_{Sup}}) - \sin(\theta_{LP_{inf}})) \tag{4.5}$$

where F_L is the compressive force of the follower load, and $\theta_{LP_{Sup}}$ and $\theta_{LP_{Sup}}$ represent the load-path inferior and superior to the eyelet (e.g. for L5 $\theta_{LP_{Sup}}$ and $\theta_{LP_{Sup}}$ are $\theta_{LP_{01}}$ and $\theta_{LP_{12}}$).

Another free-body diagram is used to calculate the total moments (M_{23}, M_{12}, M_{01}), including the follower load at the IAR as

$$\sum M = M_{23} + M_{43} - a_3 R_3 F_{3x}\cos(\theta_3) + a_3 R_3 F_{3y}\sin(\theta_3) = 0 \tag{4.6}$$

$$\sum F_y = F_{3y} + R_{43y} + R_{23y} = 0 \tag{4.7}$$

$$\sum F_x = F_{3x} + R_{43x} + R_{23x} = 0 \tag{4.8}$$

$$\begin{aligned}\sum M &= M_{12} + M_{32} - a_2 R_2 F_{2x}\cos(\theta_2) + a_2 R_2 F_{2y}\sin(\theta_2) \\ &- R_2 R_{32x}\cos(\theta_2) + R_2 R_{32y}\sin(\theta_2) = 0\end{aligned} \tag{4.9}$$

$$\sum F_y = F_{2y} + R_{32y} + R_{12y} = 0 \tag{4.10}$$

$$\sum F_x = F_{2x} + R_{32x} + R_{12x} = 0 \tag{4.11}$$

$$\begin{aligned}\sum M &= M_{01} + M_{21} - a_1 R_1 F_{1x}\cos(\theta_1) + a_1 R_1 F_{1y}\sin(\theta_1) \\ &- R_1 R_{21x}\cos(\theta_1) + R_1 R_{21y}\sin(\theta_1) = 0\end{aligned} \tag{4.12}$$

$$\sum F_y = F_{1y} + R_{21y} + R_{01y} = 0 \tag{4.13}$$

$$\sum F_x = F_{1x} + R_{21x} + R_{01x} = 0 \tag{4.14}$$

Solving for the moments at the IAR yields

$$M_{23} = M_{in} + a_3 R_3 F_{3x}\cos(\theta_3) - a_3 R_3 F_{3y}\sin(\theta_3) \tag{4.15}$$

$$\begin{aligned}M_{12} &= M_{23} + a_2 R_2 F_{2x}\cos(\theta_2) - a_2 R_2 F_{2y}\sin(\theta_2) \\ &+ R_2 F_{3x}\cos(\theta_2) - R_2 F_{3y}\sin(\theta_2)\end{aligned} \tag{4.16}$$

$$\begin{aligned}M_{01} &= M_{12} + R_1 a_1 F_{1x}\cos(\theta_1) - R_1 a_1 F_{1y}\sin(\theta_1) \\ &+ R_1(F_{2x} + F_{3x})\cos(\theta_1) - R_1(F_{2y} + F_{3y})\sin(\theta_1)\end{aligned} \tag{4.17}$$

Table 4.1: Parametrized values for the moment-rotation response.

Conditions	Level	$m_{o_{loading}}$	$\alpha_{loading}$	$m_{o_{unloading}}$	$\alpha_{unloading}$	A	B
Intact	L5-S1	-1.46	0.43	-2.62	0.34	-7.71	3.49
	L4-L5	2.96	0.47	1.47	0.45	-2.13	6.49
	L3-L4	3.68	0.44	2.58	0.37	-1.48	8.58
Fused	L4-L5	-23.7	0.10	9.16	-0.70	-3.74	0.16
FlexBAC	L4-L5	2.86	0.78	0.43	0.66	-1.23	5.22

4.2.2 Model Verification

Model verification occurred through multilevel (L3-S1) cadaveric tests under three conditions: intact, simulated fusion using surgical plates and rods at L4-L5 (fused), and implanted at L4-L5 with the FlexBAC [1], a prototype TDR (Crocker Spinal Technologies, Park City, UT). All conditions were tested under a compressive follower load of 440 N with optical markers attached to determine the moment-rotation response of each individual FSU in flexion-extension. Pedicle screws were attached prior to the testing of the intact spine. L4-L5 was then fused, and the moment-rotation response was measured again. The fusion system was replaced with the FlexBAC and the resulting moment-rotation response was determined.

The PRBM was used to predict the global moment-rotation response of the three cases. Spring stiffness values associated with L5-S1 and L3-L4 were obtained from data collected during testing of the intact case. The moment-rotation response of L4-L5 used in the PRBM was determined from the data collected during their respective cases. The moment-rotation responses for the PRBM were fit to the equation

$$\frac{A-B}{1+e^{\alpha(m-m_o)}}+B=\theta \tag{4.18}$$

by a least-squares method. Values for A, B, α, and m_o are shown in Table 4.1. Results typical of this fit are shown in Figure 4.2.

The global moment-rotation response obtained in-vitro was then compared with the moment-rotation response obtained through the PRBM.

The relative motion of each FSU was determined using both the PRBM and in-vitro testing. The ratio of motion of each FSU to the global motion was also examined.

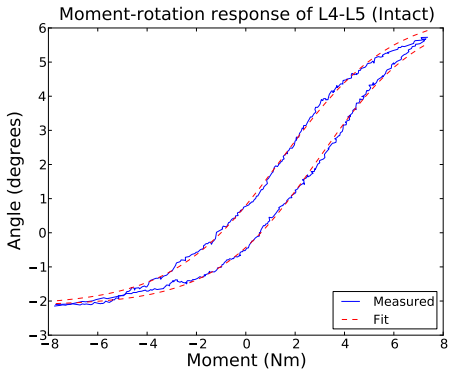

Figure 4.2: Typical numerical fit of the moment-rotation response.

Finally, the PRBM was used to determine the stiffness of adjacent segments. In this procedure, the known moment-rotation response of the implanted segment and the rotations obtained via optical tracking were used to calculate the moment applied to the implanted segment. These values were then used with the PRBM to predict the moment applied to adjacent segments. The applied moment and rotation obtained through optical tracking were then used to determine the moment-rotation response of adjacent segments.

4.3 Results

4.3.1 Global motion

The predicted (and measured) ranges of motion for flexion in the intact, fused, and implanted cases were 15.4° (15.3°), 9.5° (10.5°), and 15.2° (14.8°), respectively. The range of motion in extension were 9.5° (9.5°), 8.0° (8.1°), 8.8° (7.8°). The global moment-rotation response of the entire specimen (L3-S1) was graphically compared to the motion predicted by the PRBM (Figure 4.3). As demonstrated in Figures 4.3(b) and 4.3(a) the range of motion is decreased through the fusion of one level. Figure 4.3(c) demonstrates that the TDR provides a similar moment-rotation response in flexion, yet limits the range of motion in extension by approximately 2°. The results also demonstrate that the PRBM provides an estimation of the global moment-rotation response.

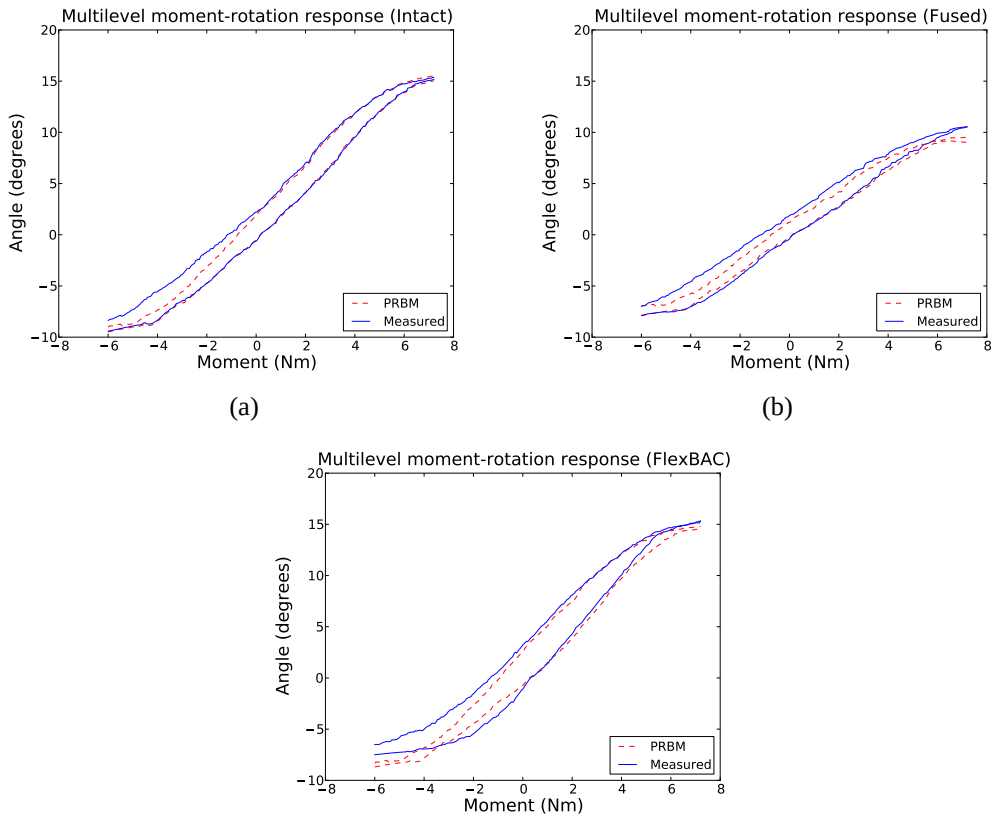

Figure 4.3: The moment-rotation response of the spine (L3-S1) for the (a) intact, (b) fused, and (c) implanted cases.

4.3.2 Relative Motion

An example of the agreement of the relative motion at the operative and adjacent levels predicted by the PRBM and measured through cadaveric testing are shown in Figure 4.4. Figure 4.4(a) and Figure 4.4(b) show that the fusion of L4-L5 results in exaggerated movement of L3-L4, characteristic of a hypermobile segment. The implanted segment was shown to have a similar relative motion pattern as that of the intact segment.

4.3.3 Deterministic Modeling

The moment-rotation response determined through the PRBM and the measured response of L5-S1 with the FlexBAC implanted is shown in Figure 4.5. Results at other levels and conditions were similar.

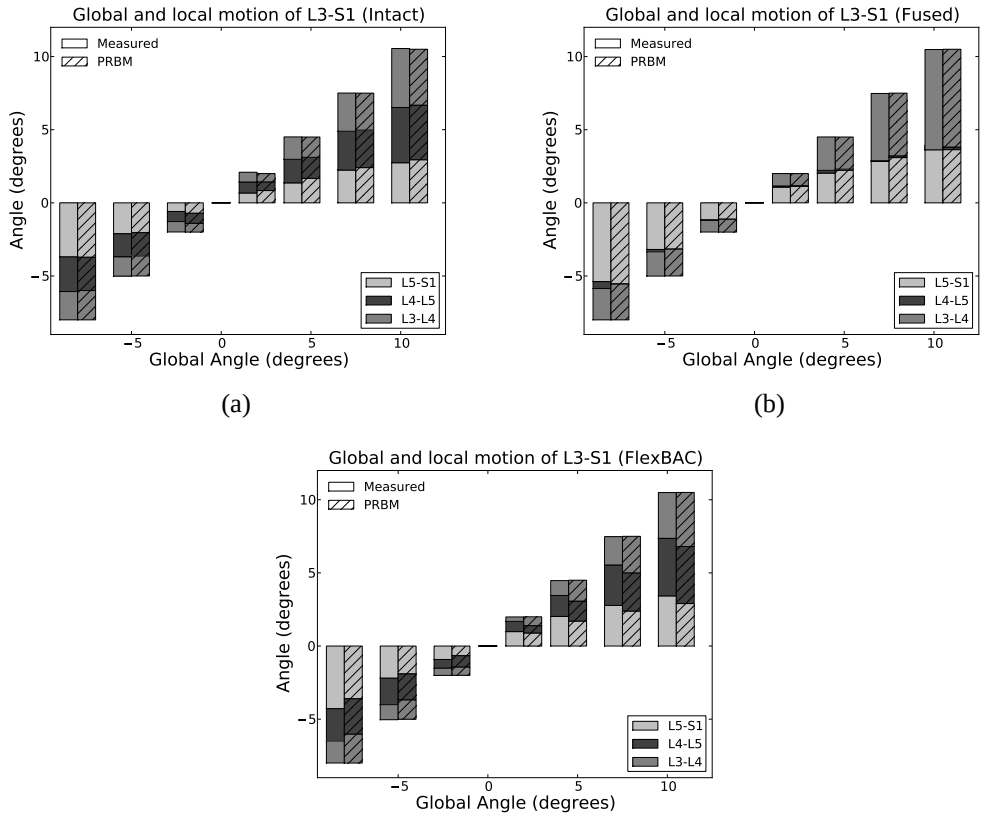

Figure 4.4: The percent motion of segment L3-L4 under the (a) intact, (b) fused, and (c) implanted conditions.

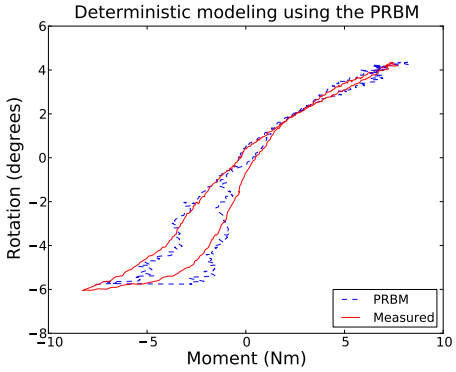

Figure 4.5: The calculated and actual moment-rotation response of L5-S1 with the FlexBAC implanted.

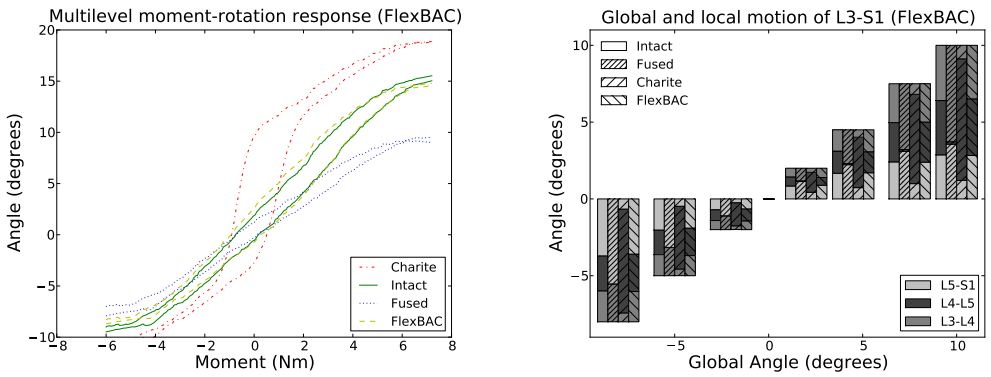

(a) (b)

Figure 4.6: Comparison of the impact of different procedures on (a) global motion patterns and (b) relative motion.

4.4 Discussion

The PRBM showed fidelity with data acquired in-vitro. The PRBM was able to accurately determine the global moment-rotation response in all three cases: intact, fused, and implanted. The range of motion was also accurately predicted. Although this work only demonstrated the use of the PRBM in flexion-extension, similar principles apply to lateral bending and axial rotation. Using the PRBM to predict global motion patterns may be useful in the early design stages where it would be useful to know the effect of the implant on surrounding motion patterns.

The PRBM also demonstrated the ability to accurately predict the relative changes in motion of the adjacent segments. The model was able to predict both the trend as well as the relative motion. Additionally, the PRBM was also able to provide an estimate of the moment rotation response of the adjacent segments. However, the resultant model was "noisy" because of measurement and numerical error. The "noise" could possibly be reduced through the use of filtering.

Another possible use of the PRBM is to predict the impact that procedures such as spinal fusion, total disc replacement, or posterior dynamic stabilization systems may have on adjacent segments. An example of this technique is shown in Figure 4.6. The effect of three spinal instrumentation systems are evaluated: the Charité (a TDR whose moment-rotation response has been reported [55]), spinal fusion, and the FlexBAC. As demonstrated in Figure 4.6, when compared to the intact condition, motion at adjacent levels is amplified under the fused condition (hypermobility), reduced when implanted with the Charité (hypomobility), and very similar when implanted

with the FlexBAC. The effects of a single moment-rotation response on multiple spines could similarly be investigated.

Typically, the sooner in the design process that a concept can be evaluated the more cost effective the design becomes. The current techniques used to evaluate designs, such as animal models, in vitro testing, and finite-element models, typically occur after a physical or computer prototype has been developed. As a result, these evaluations often occur later in the design process when changes are more difficult and costly.

The PRBM offers a cost effective, accurate, and early-stage method to evaluate designs. The straightforward nature of the PRBM means that it may be used as early as a mathematical equation is available to describe the device function. This may be done before committing the time and cost needed to fabricate and test a physical prototype or create and validate an FEA model.

4.5 Conclusions

The pseudo-rigid-body model accurately predicted changes to the motion patterns of adjacent segments. When used early in the design phase, the PRBM has the potential to reduce costs and increase performance of spinal devices. Other evaluation techniques may then be used later to improve the fidelity of the model while keeping costs down. When used properly, this design approach has the potential to reduce cost and time to market of spinal instrumentation and to improve the outcomes for adjacent segments.

CHAPTER 5. CONCLUSION

The long-term success of spinal devices and procedures, used in the treatment of lower back pain, depends strongly on biomechanics. Improper biomechanics may lead to premature degeneration of adjacent levels as well as the degeneration of the surrounding tissue at the operative level. The ability to model the biomechanical changes that result from surgery and instrumentation can facilitate the design of a device that mitigates these effects. Additionally, the successful design of an implant capable of replicating the biomechanics of the human spine has the potential to alleviate lower back pain as well as the costs associated with its treatment.

This dissertation has provided modeling tools for the development of a contact-aided compliant-mechanism-based spinal arthoplasty device capable of mimicking the complex biomechanics of the human spine. Bench-top and single-level cadaveric testing have demonstrated that the performance of the device closely matches the closed-form numerical model. This work has also demonstrated, through multi-level cadaveric testing, that the device reduces the effects on adjacent levels.

Additionally, this dissertation has provided modeling tools to predict adjacent-level effects in the early-stage design process. The model was verified through the use of multi-level testing and demonstrated a high fidelity. When used in the early-stage design phase, the pseudo-rigid-body model has the potential to reduce the cost and time required to develop implants.

5.1 Summary of Contributions

The primary contributions of this work are as follows:

- The development and modeling of the spinal implant.
- The testing and validation of the spinal implant.
- Development of an accessible predictive model for adjacent level effects.

- Development of a deterministic model for evaluation of adjacent level stiffness.
- Testing and validation of the predictive and deterministic models

5.2 Suggested Future Work

Additional research is needed into the development of the FlexBAC. While the device has a theoretical wear-free motion, this quality has not yet been demonstrated. Additional tests should be performed to evaluate the wear characteristics of the device. An evaluation of the device's surgical robustness is also needed. Finally, short- and long-term fixation methods should be investigated.

While the FlexBAC was capable of providing motion in flexion-extension and left-lateral bending to within 6% of the intact case, the stiffness of the disc in axial rotation was increased by 33%. Additional work should investigate the torsional properties of the FlexBAC and rolling-contact joints in general. By introducing rotational compliance into the rolling center, the end-plates, or both, the rotational stiffness of the device may be made to match that of the natural FSU.

While this research has focused primarily on the use of compliant mechanisms as the "motion engine" of spinal arthroplasty devices, compliant mechanisms may have further use as structures within the disc space. Traditionally, the bone/implant interface of orthopedic implants has been very stiff. However, a stiff interface may cause stress-shielding and resorption of the bone. The use of compliant mechanisms in the design of the bone/implant interface may provide for a more natural distribution of load and prevent bone remodeling.

Possible future directions for this research include the investigation of the use of the pseudo-rigid-body model in clinical applications. While the PRBM has been demonstrated as a tool to evaluate spinal instrumentation and surgery, there is the possibility that the PRBM could also be used to evaluate the stiffness of adjacent segments in vivo. This evaluation could be through the implantation of a device of known stiffness, or through the evaluation of motion patterns of an already implanted device of known stiffness. This method may aid in the selection of future devices. Additional research should also be focused on modeling multi-axial motion patterns within the spinal column using the PRBM.

Finally, this research is based around the assumption that replication of the proper biomechanical response of the spine is necessary for good long-term clinical results [57, 62–64]. This assumption should be verified through clinical studies. Additionally, as the levels adjacent to a total disc replacement will degenerate naturally due to age, the effects of aging on the performance of TDRs should also be investigated.

REFERENCES

[1] Halverson, P., Howell, L., and Bowden, A., 2008. "A flexure-based bi-axial contact-aided compliant mechanism for spinal arthroplasty." In *Proceedings of the 32nd Annual Mechanisms & Robotics Conference*, pp. DETC2008–50121. 1, 13, 38

[2] Frank, J. W., Kerr, M. S., Brooker, A. S., DeMaio, S. E., Maetzel, A., Shannon, H. S., Sullivan, T. J., Norman, R. W., and Wells, R. P., 1996. "Disability resulting from occupational low back pain. part i: What do we know about primary prevention? a review of the scientific evidence on prevention before disability begins." *Spine,* **21**(24), Dec., pp. 2908–17. 1

[3] Anderson, C. K., Chaffin, D. B., Herrin, G. D., and Matthews, L. S., 1985. "A biomechanical model of the lumbosacral joint during lifting activities." *J Biomech,* **18**(8), pp. 571–84. 3

[4] Tawckoli, W., 2006. "Characterization of the three-dimensional kinematics and failure of human spinal segments." PhD thesis, Rice University. 3

[5] Marras, W. S., and Sommerich, C. M., 1991. "A three-dimensional motion model of loads on the lumbar spine: I. model structure." *Hum Factors,* **33**(2), Apr., pp. 123–37.

[6] Marras, W. S., and Sommerich, C. M., 1991. "A three-dimensional motion model of loads on the lumbar spine: II. model validation." *Hum Factors,* **33**(2), Apr., pp. 139–49.

[7] Dolan, P., Kingma, I., van Dieen, J., de Looze, M. P., Toussaint, H. M., Baten, C. T., and Adams, M. A., 1999. "Dynamic forces acting on the lumbar spine during manual handling. can they be estimated using electromyographic techniques alone?." *Spine,* **24**(7), Apr., pp. 698–703. 3

[8] Kurtz, S. M., and Edidin, A. A., eds., 2006. *Spine Technology Handbook.* Elsevier. 3

[9] Edwards, W. T., Hayes, W. C., Posner, I., 3rd White, A. A., and Mann, R. W., 1987. "Variation of lumbar spine stiffness with load." *J Biomech Eng,* **109**(1), Feb., pp. 35–42. 3

[10] Nachemson, A., 1966. "The load on lumbar disks in different positions of the body." *Clin Orthop Relat Res,* **45**, Apr., pp. 107–22. 3

[11] Nachemson, A. L., 1981. "Disc pressure measurements." *Spine,* **6**(1), Feb., pp. 93–7. 3

[12] Wilke, H. J., Neef, P., Caimi, M., Hoogland, T., and Claes, L. E., 1999. "New in vivo measurements of pressures in the intervertebral disc in daily life." *Spine,* **24**(8), Apr., pp. 755–62. 3

[13] Allbrook, D., 1957. "Movements of the lumbar spinal column." *J Bone Joint Surg Br,* **39-B**(2), May, pp. 339–45.

[14] Froning, E. C., and Frohman, B., 1968. "Motion of the lumbosacral spine after laminectomy and spine fusion. correlation of motion with the result." *J Bone Joint Surg Am,* **50**(5), July, pp. 897–918.

[15] Clayson, S. J., Newman, I. M., Debevec, D. F., Anger, R. W., Skowlund, H. V., and Kottke, F., 1962. "Evaluation of mobility of hip and lumbar vertebrae of normal young women." *Arch Phys Med Rehabil,* **43**, Jan., pp. 1–8.

[16] Hayes, M. A., Howard, T. C., Gruel, C. R., and Kopta, J. A., 1989. "Roentgenographic evaluation of lumbar spine flexion-extension in asymptomatic individuals." *Spine,* **14**(3), Mar., pp. 327–31.

[17] Tanz, S. S., 1953. "Motion of the lumbar spine, and a roentgenologic study." *Am J Roentgenol Radium Ther Nucl Med,* **69**(3), Mar., pp. 399–412. 4

[18] Panjabi, M. M., and White, A. A., 1990. *Clinical Biomechanics of the Spine*. Lippincott. 4

[19] Ochia, R. S., Inoue, N., Renner, S. M., Lorenz, E. P., Lim, T., Andersson, G. B. J., and An, H. S., 2006. "Three-dimensional in vivo measurement of lumbar spine segmental motion." *Spine,* **31**(18), Aug., pp. 2073–8.

[20] Pearcy, M., Portek, I., and Shepherd, J., 1984. "Three-dimensional x-ray analysis of normal movement in the lumbar spine." *Spine,* **9**(3), Apr., pp. 294–7. 4, 5

[21] Yamamoto, I., Panjabi, M. M., Crisco, T., and Oxland, T., 1989. "Three-dimensional movements of the whole lumbar spine and lumbosacral joint." *Spine,* **14**(11), Nov., pp. 1256–1260. 4, 24

[22] Pearcy, M. J., and Tibrewal, S. B., 1984. "Axial rotation and lateral bending in the normal lumbar spine measured by three-dimensional radiography." *Spine,* **9**(6), Sept., pp. 582–7. 4

[23] Bowden, A. E., Rundell, S., Auerbach, J., and Balderston, R., 2007. "Total disc repacement changes facet stresses in extension, lateral bending, and axial rotation." In *Spine Arthroplasty Summit 7*. 4

[24] Gertzbein, S. D., Seligman, J., Holtby, R., Chan, K. W., Ogston, N., Kapasouri, A., and Tile, M., 1986. "Centrode characteristics of the lumbar spine as a function of segmental instability." *Clin Orthop Relat Res*(208), July, pp. 48–51.

[25] Ogston, N. G., King, G. J., Gertzbein, S. D., Tile, M., Kapasouri, A., and Rubenstein, J. D., 1986. "Centrode patterns in the lumbar spine. baseline studies in normal subjects." *Spine,* **11**(6), Aug., pp. 591–5.

[26] Gertzbein, S. D., Chan, K. H., Tile, M., Seligman, J., and Kapasouri, A., 1985. "Moire patterns: an accurate technique for determination of the locus of the centres of rotation." *J Biomech,* **18**(7), pp. 501–9.

[27] Gertzbein, S. D., Holtby, R., Tile, M., Kapasouri, A., Chan, K. W., and Cruickshank, B., 1984. "Determination of a locus of instantaneous centers of rotation of the lumbar disc by moire fringes. a new technique." *Spine,* **9**(4), June, pp. 409–13.

[28] Kettler, A., Marin, F., Sattelmayer, G., Mohr, M., Mannel, H., Dürselen, L., Claes, L., and Wilke, H. J., 2004. "Finite helical axes of motion are a useful tool to describe the three-dimensional in vitro kinematics of the intact, injured and stabilised spine." *European Spine Journal: Official Publication of the European Spine Society, the European Spinal Deformity Society, and the European Section of the Cervical Spine Research Society,* **13**(6), Oct., pp. 553–559. 4, 26

[29] Oxland, T. R., Panjabi, M. M., and Lin, R. M., 1994. "Axes of motion of thoracolumbar burst fractures." *J Spinal Disord,* **7**(2), Apr., pp. 130–8. 5

[30] Haberl, H., Cripton, P. A., Orr, T., Beutler, T., Frei, H., Lanksch, W. R., and Nolte, L., 2004. "Kinematic response of lumbar functional spinal units to axial torsion with and without superimposed compression and flexion/extension." *Eur Spine J,* **13**(6), Oct., pp. 560–6. 5

[31] Zhu, Q., Larson, C. R., Sjovold, S. G., Rosler, D. M., Keynan, O., Wilson, D. R., Cripton, P. A., and Oxland, T. R., 2007. "Biomechanical evaluation of the total facet arthroplasty system: 3-dimensional kinematics." *Spine,* **32**(1), Jan., pp. 55–62. 5, 19

[32] Adams, M. A., McNally, D. S., and Dolan, P., 1996. "'Stress' distributions inside intervertebral discs. the effects of age and degeneration." *J Bone Joint Surg Br,* **78**(6), Nov., pp. 965–72. 6

[33] Cannon, J. R., and Howell, L. L., 2005. "A compliant contact-aided revolute joint." *Mechanism and Machine Theory,* **40**(11), Nov., pp. 1273–1293.

[34] Kennedy, J. A., Howell, L. L., and Greenwood, W., 2007. "Compliant high-precision equintet ratcheting (CHEQR) mechanism for safety and arming devices." *Precision Engineering,* **31**(1), Jan., pp. 13–21. 7, 24

[35] Culpepper, M. L., DiBiasio, C. M., Panas, R. M., Magleby, S., and Howell, L. L., 2006. "Simulation of a carbon nanotube-based compliant parallel-guiding mechanism: A nanomechanical building block." *Applied Physics Letters,* **89**, p. 203111.

[36] Wittwer, J. W., Baker, M. S., and Howell, L. L., 2006. "Robust design and model validation of nonlinear compliant micromechanisms." *Microelectromechanical Systems, Journal of,* **15**(1), p. 33–41. 7

[37] Weight, B. L., Mattson, C. A., Magleby, S. P., and Howell, L. L., 2007. "Configuration selection, modeling, and preliminary testing in support of constant force electrical connectors." *TRANSACTIONS-AMERICAN SOCIETY OF MECHANICAL ENGINEERS JOURNAL OF ELECTRONIC PACKAGING,* **129**(3), p. 236.

[38] Wilcox, D. L., and Howell, L. L., 2005. "Fully compliant tensural bistable micromechanisms (FTBM)." *Microelectromechanical Systems, Journal of,* **14**(6), p. 1223–1235. 7

[39] Howell, L. L., 2001. *Compliant Mechanisms*. Wiley-Interscience. 7, 24, 27, 32

[40] Mankame, N. D., and Ananthasuresh, G. K., 2004. "Topology optimization for synthesis of contact-aided compliant mechanisms using regularized contact modeling." *Computers and Structures,* **82**(15-16), p. 1267–1290.

[41] Kirsch, U., 1989. "Optimal topologies of structures." *Applied Mechanics Reviews,* **42**(8), p. 223–239.

[42] Sigmund, O., 1997. "On the design of compliant mechanisms using topology optimization." *Mechanics Based Design of Structures and Machines,* **25**(4), p. 493–524. 7

[43] Guerinot, A. E., Magleby, S. P., Howell, L. L., and Todd, R. H., 2005. "Compliant joint design principles for high compressive load situations." *Journal of Mechanical Design,* **127**, p. 774. 7

[44] Mankame, N. D., and Ananthasuresh, G. K., 2002. "Contact aided compliant mechanisms: concept and preliminaries." *ASME Design Engineering and Technical Conference, pp. MECH–34211,(Montreal).* 7

[45] Cannon, J. R., Lusk, C. P., and Howell, L. L., 2005. "Compliant rolling-contact element mechanisms." *Proceedings of the 2005 ASME Design Engineering Technical Conferences*. 26

[46] Halverson, P., Magleby, S., Jensen, B., and Howell, L., 2007. "Concepts for achieving multistability in compliant rolling-contact elements." In *Proceedings of the 31st Annual Mechanisms & Robotics Conference*, pp. DETC2007–4836. 26

[47] Halverson, P. A., 2007. "Compliant rolling-contact elements." PhD thesis, Brigham Young University, Provo, Ut. 7, 8

[48] Cadman, R. V., 1970. Rolamite: Geometry and force analysis. Tech. rep., SC-RR–68-223, Sandia Labs., Albuquerque, N. Mex. 8

[49] Hillberry, B. M., and Allen S. Hall, J., 1976. United states patent: 3945053 - rolling contact prosthetic knee joint, Mar. 7

[50] Jeanneau, A., Herder, J., Laliberte, T., and Gosselin, C., 2004. "A compliant rolling contact joint and its application in a 3-dof planar parallel mechanism with kinematic analysis." In *Proceedings of the 38th Annual Mechanisms & Robotics Conference*, pp. DETC2004–57264. 7, 8

[51] Chironis, N. P., and Sclater, N., 1991. *Mechanisms and Mechanical Devices Sourcebook*. McGraw-Hill, New York. 7

[52] Kirkaldy-Willis, W. H., Wedge, J. H., Yong-Hing, K., and Reilly, J., 1978. "Pathology and pathogenesis of lumbar spondylosis and stenosis." *Spine,* **3**(4), Dec., pp. 319–28. 9

[53] Park, P., Garton, H. J., Gala, V. C., Hoff, J. T., and McGillicuddy, J. E., 2004. "Adjacent segment disease after lumbar or lumbosacral fusion: review of the literature." *Spine,* **29**(17), Sept., pp. 1938–1944. 9, 33

[54] Cinotti, G., David, T., and Postacchini, F., 1996. "Results of disc prosthesis after a minimum follow-up period of 2 years." *Spine,* **21**(8), Apr., pp. 995–1000. 9

[55] O'Leary, P., Nicolakis, M., Lorenz, M. A., Voronov, L. I., Zindrick, M. R., Ghanayem, A., Havey, R. M., Carandang, G., Sartori, M., Gaitanis, I. N., Fronczak, S., and Patwardhan,

A. G., 2007. “Response of charité total disc replacement under physiologic loads: prosthesis component motion patterns.” *The Spine Journal,* **5**(6), Nov., pp. 590–599. 9, 24, 42

[56] Hallab, N. J., Cunningham, B. W., and Jacobs, J. J., 2003. “Spinal implant debris-induced osteolysis.” *Spine,* **28**(20), Oct., pp. S125–38. 9

[57] Kostuik, J. P., 1997. “Intervertebral disc replacement. experimental study..” *Clin. Orthop. Relat. Res.,* **337**, pp. 27–41. 1, 46

[58] Hedman, T. P., Kostuik, J. P., Fernie, G. R., and Maki, B. E., 1988. United states patent: 4759769 - artificial spinal disc, July. 10

[59] Urbaniak, J. R., Bright, D. S., and Hopkins, J. E., 1973. “Replacement of intervertebral discs in chimpanzees by silicone-dacron implants: a preliminary report..” *J. Biomed. Mater. Res.,* **7**, pp. 165–186.

[60] Stubstad, J. A., Urbaniak, J. R., and Kahn, P., 1975. United states patent: 3867728 - prosthesis for spinal repair, Feb.

[61] Lee, C. K., Langrana, N. A., Alexander, H., Clemow, A. J., Chen, E. H., and Parsons, J. R., 1990. United states patent: 4911718 - functional and biocompatible intervertebral disc spacer, Mar. 10

[62] Lee, C. K., and Langrana, N. A., 1984. “Lumbosacral spinal fusion. a biomechanical study.” *Spine,* **9**(6), Sept., pp. 574–581.

[63] Weinhoffer, S. L., Guyer, R. D., Herbert, M., and Griffith, S. L., 1995. “Intradiscal pressure measurements above an instrumented fusion. a cadaveric study.” *Spine,* **20**(5), Mar., pp. 526–531.

[64] Nagata, H., Schendel, M. J., Transfeldt, E. E., and Lewis, J. L., 1993. “The effects of immobilization of long segments of the spine on the adjacent and distal facet force and lumbosacral motion.” *Spine,* **18**(16), Dec., pp. 2471–2479. 23

[65] Zigler, J., 2004. “Lumbar spine arthroplasty using the ProDisc II.” *The Spine Journal,* **4**(6), pp. S260–S267.

[66] Guyer, R. D., Tromanhauser, S. G., and Regan, J. J., 2007. “An economic model of one-level lumbar arthroplasty versus fusion.” *The Spine Journal,* **7**(5), pp. 558–562. 23

[67] Shim, C. S., Lee, S., Shin, H., Kang, H. S., Choi, W., Jung, B., Choi, G., Ahn, Y., Lee, S., and Lee, H. Y., 2007. “CHARITE versus ProDisc: a comparative study of a minimum 3-year follow-up.” *Spine,* **32**(9), Apr., pp. 1012–1018. 24

[68] Huang, R. C., Girardi, F. P., Jr, F. P. C., Tropiano, P., and Marnay, T., 2003. “Long-term flexion-extension range of motion of the prodisc total disc replacement.” *Journal of Spinal Disorders & Techniques,* **16**(5), Oct., pp. 435–440.

[69] Huang, R. C., Girardi, F. P., Cammisa, F. P., Lim, M. R., Tropiano, P., and Marnay, T., 2005. “Correlation between range of motion and outcome after lumbar total disc replacement: 8.6-Year follow-up.” *Spine,* **30**(12), pp. 1407–1411. 23

[70] Dooris, A. P., Goel, V. K., Grosland, N. M., Gilbertson, L. G., and Wilder, D. G., 2001. "Load-sharing between anterior and posterior elements in a lumbar motion segment implanted with an artificial disc." *Spine,* **26**(6), Mar., pp. E122–129.

[71] Schmidt, H., Heuer, F., and Wilke, H., 2008. "Interaction between finite helical axes and facet joint forces under combined loading." *Spine,* **33**(25), Dec., pp. 2741–2748. 23, 25, 26

[72] Jun, S., Lee, K., Park, C., and Lee, S., 2008. "Changes in center of rotation and facet loads of the lumbar motion segment following total disc replacement." In *Proceedings of the 8th Annual Meeting of the Spinal Arthroplasty Society*, p. P32. 24

[73] Stokes, I. A. F., and Iatridis, J. C., 2004. "Mechanical conditions that accelerate intervertebral disc degeneration: overload versus immobilization." *Spine,* **29**(23), pp. 2724–2732. 24, 31, 33

[74] Rundell, S. A., Auerbach, J. D., Balderston, R. A., and Kurtz, S. M., 2008. "Total disc replacement positioning affects facet contact forces and vertebral body strains." *Spine,* **33**(23), Nov., pp. 2510–2517. 24

[75] Roach, G. M., and Howell, L. L., 2002. "Evaluation and comparison of alternative compliant overrunning clutch designs." *Journal of Mechanical Design,* **124**(3), pp. 485–491. 24

[76] Motsinger, R., and Stien, P., 1964. "Flexural devices in measurement systems." In *Measurement Engineering*. Stein Engineering Services, Phoenix, AZ. 24

[77] Hopkins, J. B., and Culpepper, M. L., 2010. "Synthesis of multi-degree of freedom, parallel flexure system concepts via freedom and constraint topology (FACT) - part i: Principles." *Precision Engineering,* **34**(2), pp. 259–270.

[78] Parise, J. J., Howell, L. L., and Magleby, S. P., 2001. "Ortho-planar linear-motion springs." *Mechanism and Machine Theory,* **36**(11-12), Nov., pp. 1281–1299.

[79] Ananthasuresh, G., and Kota, S., 1995. "Designing compliant mechanisms.." *Mechanical Engineering,* **117**(3), pp. 93–96. 24

[80] Halverson, P. A., Howell, L. L., and Magleby, S. P., 2010. "Tension-based multi-stable compliant rolling-contact elements." *Mechanism and Machine Theory,* **45**(2), Feb., pp. 147–156. 26

[81] , 2003. Standard test methods for spinal implant constructs in a vertebrectomy model Tech. Rep. ASTM F1717 - 09, ASTM International, West Conshohocken, PA. 27

[82] Goertzen, D. J., Lane, C., and Oxland, T. R., 2004. "Neutral zone and range of motion in the spine are greater with stepwise loading than with a continuous loading protocol. an in vitro porcine investigation." *Journal of Biomechanics,* **37**(2), Feb., pp. 257–261. 28

[83] Patwardhan, A. G., Havey, R. M., Meade, K. P., Lee, B., and Dunlap, B., 1999. "A follower load increases the load-carrying capacity of the lumbar spine in compression." *Spine,* **24**(10), May, pp. 1003–1009. 28, 35

[84] Söderkvist, I., and Åke Wedin, P., 1993. "Determining the movements of the skeleton using well-configured markers." *Journal of Biomechanics*, **26**(12), Dec., pp. 1473–1477. 28

[85] Bowden, A. E., Guerin, H. L., Villarraga, M. L., Patwardhan, A. G., and Ochoa, J. A., 2008. "Quality of motion considerations in numerical analysis of motion restoring implants of the spine." *Clinical Biomechanics*, **23**(5), June, pp. 536–544. 31

[86] Frost, H. M., 1998. "From wolff's law to the mechanostat: a new "face" of physiology." *Journal of Orthopaedic Science: Official Journal of the Japanese Orthopaedic Association*, **3**(5), pp. 282–286. 33

[87] Cramer, G. D., Fournier, J. T., Henderson, C. N. R., and Wolcott, C. C., 2004. "Degenerative changes following spinal fixation in a small animal model." *Journal of Manipulative and Physiological Therapeutics*, **27**(3), Apr., pp. 141–154. 33

[88] Alini, M., Eisenstein, S. M., Ito, K., Little, C., Kettler, A. A., Masuda, K., Melrose, J., Ralphs, J., Stokes, I., and Wilke, H. J., 2008. "Are animal models useful for studying human disc disorders/degeneration?." *European Spine Journal*, **17**(1), Jan., pp. 2–19. 34

[89] Shirazi-Adl, A., Ahmed, A. M., and Shrivastava, S. C., 1986. "A finite element study of a lumbar motion segment subjected to pure sagittal plane moments." *Journal of Biomechanics*, **19**(4), pp. 331–350. 34

[90] Shirazi-Adl, A., 1991. "Finite-element evaluation of contact loads on facets of an L2-L3 lumbar segment in complex loads." *Spine*, **16**(5), May, pp. 533–541.

[91] Shirazi-Adl, A., 1994. "Biomechanics of the lumbar spine in sagittal/lateral moments." *Spine*, **19**(21), Nov., pp. 2407–2414. 34

[92] Shirazi-Adl, A., El-Rich, M., Pop, D. G., and Parnianpour, M., 2005. "Spinal muscle forces, internal loads and stability in standing under various postures and loads–application of kinematics-based algorithm." *European Spine Journal: Official Publication of the European Spine Society, the European Spinal Deformity Society, and the European Section of the Cervical Spine Research Society*, **14**(4), May, pp. 381–392. 34

[93] Bergmark, A., 1989. "Stability of the lumbar spine – a study in mechanical engineering." *Acta Orthopaedica Scandinavica*, **60**(3 supp 230), p. 1. 34

[94] DiBiasio, C. M., Culpepper, M. L., Panas, R., Howell, L. L., and Magleby, S. P., 2008. "Comparison of molecular simulation and Pseudo-Rigid-Body model predictions for a carbon Nanotube–Based compliant Parallel-Guiding mechanism." *Journal of Mechanical Design*, **130**(4), Apr., pp. 042308–7.

[95] Mattson, C. A., Howell, L. L., and Magleby, S. P., 2004. "Development of commercially viable compliant mechanisms using the Pseudo-Rigid-Body model: Case studies of parallel mechanisms." *Journal of Intelligent Material Systems and Structures*, **15**(3), Mar., pp. 195–202. 35

[96] Patwardhan, A. G., Havey, R. M., Ghanayem, A. J., Diener, H., Meade, K. P., Dunlap, B., and Hodges, S. D., 2000. “Load-carrying capacity of the human cervical spine in compression is increased under a follower load.” *Spine*, **25**(12), June, pp. 1548–1554.

APPENDIX A. ANALYSIS OF CONTACT-AIDED MECHANISMS

This python-based program allows for quick and accurate modeling of contact-aided mechanisms using closed-form solutions. The input to the program is an Excel spreadsheet that contains the curvature of the surface and flexures.

```
import sys
from PyQt4 import QtCore, QtGui
from GUI_inter import Ui_MainWindow
import scipy as sp

import matplotlib
from matplotlib.backends.backend_qt4agg \
  import FigureCanvasQTAgg as FigureCanvas
from matplotlib.backends.backend_qt4agg \
  import NavigationToolbar2QTAgg as NavigationToolbar
from matplotlib.figure import Figure
from matplotlib.backends.backend_qt4agg \
  import NavigationToolbar2QTAgg as NavigationToolbar
import matplotlib.pyplot as plt

import numpy as np
import xlrd

def radians(x):
    return x *np.pi/180
```

```
def arclengthfunc(R_s,angle):
    arclength=[]
    i=0
    while i < (R_s.size-1):
        arclength.append(R_s[i]*radians(angle[i+1]-angle[i]))
        i +=1
    return np.array(arclength)

def compress_mom_arm(R_s,x,angles,arclength):
    Neutral_position=abs(angles).argmin()
    compression_moment=np.array([])        #Nm
    i=0
    while i < (R_s.size):

        if i < Neutral_position:
            compression_moment=np.append(compression_moment,
                     ((-arclength[i:Neutral_position].sum()+x)/1000))
        else:
            compression_moment=np.append(compression_moment,
           ((arclength[0:i].sum()-arclength[0:Neutral_position].sum()+x)/1000))
        i+=1
    return compression_moment

def calc_moment(R_s,R_ccw,R_cw,E,I_cw,I_ccw):
    T_ccw=E*I_ccw*(-2/R_ccw+1/R_s)
    T_cw=E*I_cw*(-2/R_cw+1/R_s)
    return T_ccw-T_cw
```

```
def N_func(R_s,Ro_a,E,t,Sut,Se):
    Flex_a_curve=E*t/2*(1/R_s-1/Ro_a)*10**3
    Flex_a_flat=E*t/2*(-1/Ro_a)*10**3
    sigma_a_a=abs((Flex_a_curve-Flex_a_flat)/2)
    sigma_m_a=abs((Flex_a_curve+Flex_a_flat)/2)
    N_a=Sut*Se/(Sut*sigma_a_a+Se*sigma_m_a)
    return [N_a,Flex_a_curve,Flex_a_flat]

class StartQT4(QtGui.QMainWindow):
    def __init__(self, parent=None):
        QtGui.QWidget.__init__(self, parent)
        self.ui = Ui_MainWindow()
        self.ui.setupUi(self)
        self.setWindowTitle("FlexBAC")

        #Create 1st page graph
        self.ui.dpi=100
        self.ui.fig_FD=Figure((3.6,3.4),dpi=self.ui.dpi) # FD graph
        self.ui.fig_N=Figure((3.5,3.2),dpi=self.ui.dpi) # SF  graph
        self.ui.fig_Stress=Figure((3.5,3.2),dpi=self.ui.dpi) # Sig graph
        self.ui.fig_FL=Figure((3.6,3.4),dpi=self.ui.dpi) # FL graph
        self.ui.fig_SR=Figure((3.6,3.4),dpi=self.ui.dpi) # SR graph




        self.ui.canvas_FD=FigureCanvas(self.ui.fig_FD)
        self.ui.canvas_N=FigureCanvas(self.ui.fig_N)
        self.ui.canvas_Stress=FigureCanvas(self.ui.fig_Stress)
        self.ui.canvas_FL=FigureCanvas(self.ui.fig_FL)
        self.ui.canvas_SR=FigureCanvas(self.ui.fig_SR)
```

```
self.ui.canvas_FD.setParent(self.ui.tabWidget)
self.ui.canvas_N.setParent(self.ui.tabWidget)
self.ui.canvas_Stress.setParent(self.ui.tabWidget)
self.ui.canvas_FL.setParent(self.ui.tabWidget)
self.ui.canvas_SR.setParent(self.ui.tabWidget)

#Put toolbars on all graphs

self.ui.toolbar_FD=NavigationToolbar(self.ui.canvas_FD,
                                     self.ui.tabWidget)
self.ui.toolbar_N=NavigationToolbar(self.ui.canvas_N,
                                    self.ui.tabWidget)
self.ui.toolbar_Stress=NavigationToolbar(self.ui.canvas_Stress,
                                         self.ui.tabWidget)
self.ui.toolbar_FL=NavigationToolbar(self.ui.canvas_FL,
                                     self.ui.tabWidget)
self.ui.toolbar_SR=NavigationToolbar(self.ui.canvas_SR,
                                     self.ui.tabWidget)

self.ui.FD_vbox.addWidget(self.ui.canvas_FD)
self.ui.FD_vbox.addWidget(self.ui.toolbar_FD)

self.ui.N_vbox.addWidget(self.ui.canvas_N)
self.ui.N_vbox.addWidget(self.ui.toolbar_N)

self.ui.Stress_vbox.addWidget(self.ui.canvas_Stress)
self.ui.Stress_vbox.addWidget(self.ui.toolbar_Stress)

self.ui.FL_vbox.addWidget(self.ui.canvas_FL)
```

```
        self.ui.FL_vbox.addWidget(self.ui.toolbar_FL)

        self.ui.SR_vbox.addWidget(self.ui.canvas_SR)
        self.ui.SR_vbox.addWidget(self.ui.toolbar_SR)


        self.ui.FD=self.ui.fig_FD.add_subplot(111)
        self.ui.N=self.ui.fig_N.add_subplot(111)
        self.ui.Stress=self.ui.fig_Stress.add_subplot(111)
        self.ui.FL=self.ui.fig_FL.add_subplot(111)
        self.ui.SR=self.ui.fig_SR.add_subplot(111)

        self.ui.FD.clear()
        self.ui.N.clear()
        self.ui.Stress.clear()
        self.ui.FL.clear()
        self.ui.SR.clear()


        QtCore.QObject.connect(self.ui.actionOpen,QtCore.SIGNAL("triggered()"),
                               self.file_dialog)
        QtCore.QObject.connect(self.ui.pushButton,QtCore.SIGNAL("clicked()"),
                               self.update_graphs)


    def file_dialog(self):
        global wb
        global sh
        filename=QtGui.QFileDialog.getOpenFileName(self,
                'Open File', './', "Excel Files (*.xls);; All Files (*.*)")
```

```
    #Get the first names of the columns
    wb=xlrd.open_workbook(filename)            #read in entire workbook
    sh=wb.sheet_by_index(0)                      #read 1st sheet
    n=0
    for col in range(sh.ncols):
        self.ui.comboBox.insertItem(n,sh.col_values(col)[0])
        self.ui.comboBox_2.insertItem(n,sh.col_values(col)[0])
        self.ui.comboBox_3.insertItem(n,sh.col_values(col)[0])
        self.ui.comboBox_4.insertItem(n,sh.col_values(col)[0])
        n+=1
    self.setWindowTitle("FlexBAC Design:"+filename)

def update_graphs(self):
    R_s=np.array(sh.col_values(self.ui.comboBox_3.currentIndex())[1:])
    R_ccw=np.array(sh.col_values(self.ui.comboBox.currentIndex())[1:])
    R_cw=np.array(sh.col_values(self.ui.comboBox_2.currentIndex())[1:])
    angles=np.array(sh.col_values(self.ui.comboBox_4.currentIndex())[1:])
    t=float(self.ui.b_thick.text())
    Sut=float(self.ui.b_sut.text())
    Se=float(self.ui.b_se.text())
    I_cw=float(self.ui.b_thick.text())**3*\
    float(self.ui.b_width_cw.text())/12.0
    I_ccw=float(self.ui.b_thick.text())**3*\
    float(self.ui.b_width_ccw.text())/12.0
    E=float(self.ui.b_mod.text())

    arclength=arclengthfunc(R_s,angles)
    moment=calc_moment(R_s,R_ccw,R_cw,E,I_cw,I_ccw)

    [N_ccw,Flex_ccw_curve,Flex_ccw_flat]=N_func(R_s,R_ccw,E,t,Sut,Se)
```

```
[N_cw,Flex_cw_curve,Flex_cw_flat]=N_func(R_s,R_cw,E,t,Sut,Se)


CAM=compress_mom_arm(R_s,0,angles,arclength)
self.ui.FD.clear()
self.ui.N.clear()
self.ui.Stress.clear()
self.ui.FL.clear()
self.ui.SR.clear()

self.ui.FD.plot(moment,angles)
self.ui.FD.set_xlabel('Moment (Nm)')
self.ui.FD.set_ylabel('Angle (degrees)')
self.ui.N.plot(angles,N_ccw)
self.ui.N.plot(angles,N_cw)
self.ui.N.set_ylim((0,2))

if self.ui.FL0N.isChecked():
    self.ui.FL.plot(moment+CAM*0,angles)
if self.ui.FL200N.isChecked():
    self.ui.FL.plot(moment+CAM*200,angles)
if self.ui.FL400N.isChecked():
    self.ui.FL.plot(moment+CAM*400,angles)
if self.ui.FL600N.isChecked():
    self.ui.FL.plot(moment+CAM*600,angles)
if self.ui.FL800N.isChecked():
    self.ui.FL.plot(moment+CAM*800,angles)

self.ui.FL.set_xlabel('Moment (Nm)')
self.ui.FL.set_ylabel('Angle (degrees)')
```

```
self.ui.Stress.plot(angles,Flex_ccw_flat)
self.ui.Stress.plot(angles,Flex_cw_flat)
self.ui.Stress.plot(angles, Flex_ccw_curve)
self.ui.Stress.plot(angles, Flex_cw_curve)

if self.ui.Place_1.isChecked():
    SR_moment=moment+compress_mom_arm(R_s,
                                float(self.ui.P_1.text()),
                                angles,
                                arclength)*float(self.ui.LE_FL.text())
    SR_A_o=sp.interp(0,SR_moment,angles)
    SR_angles=angles-SR_A_o
    self.ui.SR.plot(SR_moment,SR_angles)
if self.ui.Place_2.isChecked():
    SR_moment=moment+compress_mom_arm(R_s,float(self.ui.P_2.text()),
                                angles,
                                arclength)*float(self.ui.LE_FL.text())

    SR_A_o=sp.interp(0,SR_moment,angles)
    SR_angles=angles-SR_A_o
    self.ui.SR.plot(SR_moment,SR_angles)

if self.ui.Place_3.isChecked():
    SR_moment=moment+compress_mom_arm(R_s,float(self.ui.P_3.text()),
                                angles,
                                arclength)*float(self.ui.LE_FL.text())
    SR_A_o=sp.interp(0,SR_moment,angles)
    SR_angles=angles-SR_A_o
    self.ui.SR.plot(SR_moment,SR_angles)
```

```
        if self.ui.Place_4.isChecked():
            SR_moment=moment+compress_mom_arm(R_s,
                                              float(self.ui.P_4.text()),
                                              angles,
                                              arclength)*float(self.ui.LE_FL.text())
            SR_A_o=sp.interp(0,SR_moment,angles)
            SR_angles=angles-SR_A_o
            self.ui.SR.plot(SR_moment,SR_angles)

        self.ui.canvas_FD.draw()
        self.ui.canvas_Stress.draw()
        self.ui.canvas_N.draw()
        self.ui.canvas_FL.draw()
        self.ui.canvas_SR.draw()

if __name__ == "__main__":
    app = QtGui.QApplication(sys.argv)
    myapp = StartQT4()
    myapp.show()
    sys.exit(app.exec_())
```

APPENDIX B. SIMULATED RESPONSE USING THE PRBM

This python-based program allows for modeling and graphing of adjacent-level effects using the pseudo-rigid-body model. The input to this program is an Excel-based spreadsheet containing the force-deflection response of each individual level of the spine. The Excel worksheet is what defines the conditions (e.g. intact, fused, etc...).

```
import numpy as np
import xlrd
import matplotlib.pyplot as plt
import itertools
from scipy.optimize import leastsq
from Filter import savitzky_golay as sg
import matplotlib.patches as mpatches

FontSize=20
TickSize=15

def interp(x0,x,y):
    if x[0]>x[1]:
        x=x[::-1]
        y=y[::-1]
        return np.interp(x0,x,y)
    else:
        return np.interp(x0,x,y)

def local_minima(fits, window=20): #{{{
```

```
    """
    Find the local minima within fits, and return them and their indices.

    Returns a list of indices at which the minima were found, and a list of the
    minima, sorted in order of increasing minimum.  The keyword argument window
    determines how close two local minima are allowed to be to one another.  If
    two local minima are found closer together than that, then the lowest of
    them is taken as the real minimum.  window=1 will return all local minima.

    """
    if fits.__class__==np.array([]).__class__:
        fits=map(None,fits)
    from scipy.ndimage.filters import minimum_filter as min_filter

    minfits = min_filter(fits, size=window, mode="wrap")

    minima = []
    for i in range(len(fits)):
        if fits[i] == minfits[i]:
            minima.append(fits[i])

    minima.sort()

    good_indices = [ fits.index(fit) for fit in minima ]
    good_fits = [ fit for fit in minima ]

    return(good_indices, good_fits)

def evaleq(moment,p):
    T,A,mn,mx=p
```

```
    return (mx-mn)*1.0/(1+np.exp(-A*(moment-T)))+mn

def FindSwing(Moment,Angle):
    '''finds and returns the curve indicies starting at the 1st local minima to
    the 1st local maxima and the from the 1st local maxima to the second local
        minima
    '''
    maxind,values=local_minima(-Moment)
    minind,values=local_minima(Moment)
    maxind.sort()
    minind.sort()

    #=== Remove duplicates
    d = {}
    for x in maxind:
        d[x] = 1
    maxind = list(d.keys())
    d = {}
    for x in minind:
        d[x] = 1
    minind = list(d.keys())

    maxind.sort()
    minind.sort()

    if maxind[0] >= minind[0]:
        maxind=maxind[0]
    else:
        maxind=maxind[1]
```

```
    upswing=np.vstack((Moment[minind[0]:maxind],Angle[minind[0]:maxind]))
    downswing=np.vstack((Moment[maxind:minind[1]],Angle[maxind:minind[1]]))

    return upswing,downswing

def CalcfitUD(upswing,downswing):
    ''' Calculates the fit of the upswing and downswing such that
    ad=au and bd=bu'''
    Td=0.0
    Ad=.4
    Tu=0.0
    Au=.4
    mn=-3.0
    mx=3.0
    return leastsq(residUD,[Tu,Au,Td,Ad,mn,mx],args=(upswing,downswing),
                   maxfev=50000)[0]

def residUD(varlist,upswing,downswing):
    Tu,Au,Td,Ad,mn,mx=varlist
    Angle=upswing[1]
    Moment=upswing[0]
    erru=Angle-((mx-mn)*1.0/(1+np.exp(-Au*(Moment-Tu)))+mn)
    Angle=downswing[1]
    Moment=downswing[0]
    errd=Angle-((mx-mn)*1.0/(1+np.exp(-Ad*(Moment-Td)))+mn)
    return np.hstack((errd,erru))

def CalcFit(upswing,downswing):
    T=0
    A=.4
```

```
    mn=-5
    mx=8
    Tu,Au,mnu,mxu=leastsq(resid,[T,A,mn,mx],args=(upswing[0],upswing[1]),
                          maxfev=5000)[0]
    Td,Ad,mnd,mxd=leastsq(resid,[T,A,mn,mx],args=(downswing[0],downswing[1]),
                          maxfev=5000)[0]
    return Tu,Au,mnu,mxu,Td,Ad,mnd,mxd

def resid(varlist,Moment,Angle):
    T,A,mn,mx=varlist
    err=Angle-((mx-mn)*1.0/(1+np.exp(-A*(Moment-T)))+mn)
    return err

def plotfit(varlist,upswing,downswing):
    Tu,Au,mnu,mxu,Td,Ad,mnd,mxd=varlist
    plt.plot(upswing[0],evaleq(upswing[0],[Tu,Au,mnu,mxu]),'--r',label='Fit')
    plt.plot(downswing[0],evaleq(downswing[0],[Td,Ad,mnd,mxd]),'--r')

def sin(x):
    return np.sin(x*numpy.pi/180)

def cos(x):
    return np.cos(x*numpy.pi/180)

def atan2(y,x):
    return np.arctan2(y,x)*180/numpy.pi

def Calc_Load_Path(Angle,Angle_Sup,R,R_sup,ratio,ratio_sup):
    x= (1.0-ratio)*R*sin(Angle)+ratio_sup*R_sup*sin(Angle_Sup)
    y= (1.0-ratio)*R*cos(Angle)+ratio_sup*R_sup*cos(Angle_Sup)
```

```
    return atan2(y,x)

def ReadExcelWB2(filename):
# Read Data into a dictionary
    Data={}
    wb=xlrd.open_workbook(filename)
    for sheet in wb.sheet_names():
        sheet = str(sheet)
        Data[sheet]={}
        sh=wb.sheet_by_name(sheet)
        for i in range(0,sh.ncols,2):
            temp1=np.array(sh.col_values(i)[2:])
            if ((temp1=='').__class__ == np.array([]).__class__ ):
                nzero=((np.array(sh.col_values(i)[2:]))=='').nonzero()[-1][0]+2
                moment=np.array(sh.col_values(i)[2:nzero])
                angle=np.array(sh.col_values(i+1)[2:nzero])

            else :
                moment=np.array(sh.col_values(i)[2:])
                angle=np.array(sh.col_values(i+1)[2:])

            Data[sheet][str(sh.col_values(i)[0])]={}
            Data[sheet][str(sh.col_values(i)[0])][str(sh.col_values(i)[1])]=moment
            Data[sheet][str(sh.col_values(i)[0])][str(sh.col_values(i+1)[1])]=angle

    return Data

def ReadExcelWB(filename):

    Data={}
```

```
wb=xlrd.open_workbook(filename)
sh=wb.sheet_by_index(0)

for i in range(0,sh.ncols,4):
    temp1=np.array(sh.col_values(i)[2:])
    if ((temp1==’’).__class__ == np.array([]).__class__ ):
        nzero=((np.array(sh.col_values(i)[2:]))==’’).nonzero()[-1][0]+2
        moment=np.array(sh.col_values(i)[2:nzero])
        L34=np.array(sh.col_values(i+1)[2:nzero])
        L45=np.array(sh.col_values(i+2)[2:nzero])
        L51=np.array(sh.col_values(i+3)[2:nzero])

    else :
        moment=np.array(sh.col_values(i)[2:])
        L34=np.array(sh.col_values(i+1)[2:])
        L45=np.array(sh.col_values(i+2)[2:])
        L51=np.array(sh.col_values(i+3)[2:])

    Data[str(sh.col_values(i)[0])]={}
    Data[str(sh.col_values(i)[0])][str(sh.col_values(i)[1])]=moment
    Data[str(sh.col_values(i)[0])][str(sh.col_values(i+1)[1])]=L34
    Data[str(sh.col_values(i)[0])][str(sh.col_values(i+2)[1])]=L45
    Data[str(sh.col_values(i)[0])][str(sh.col_values(i+3)[1])]=L51

return Data
```

```
Data=ReadExcelWB2('./Multilevel_Norm.xls')
#
Conditions=Data.keys()
Levels=['L51','L45','L34']

Constants={}
for cond in Conditions:
    Constants[cond]={}
    for level in Data[cond].keys():
        print level,cond
        level=str(level)
        upswing,downswing=FindSwing(Data[cond][level]['Moment'],
                                    Data[cond][level]['Angle'])
        Tu,Au,Td,Ad,mn,mx=CalcfitUD(upswing,downswing)
        Constants[cond][level]=[Tu,Au,Td,Ad,mn,mx]

#======== plot fit of data for L45 Intact
def plotlevfit(level,cond):
    fig=plt.figure()
    ax=fig.add_subplot(111)
    upswing,downswing=FindSwing(Data[cond][level]['Moment'],
                                Data[cond][level]['Angle'])
    #Tu,Au,Td,Ad,mn,mx=CalcfitUD(upswing,downswing)
    Tu,Au,Td,Ad,mn,mx=Constants[cond][level]
    plt.title('Moment-rotation response of '+level+" ("+cond+')',
              fontsize=FontSize)
    plt.plot(upswing[0],upswing[1],'b',label='Measured')
    plt.plot(downswing[0],downswing[1],'b')
    plotfit([Tu,Au,mn,mx,Td,Ad,mn,mx],upswing,downswing)
    plt.xlabel('Moment (Nm)',fontsize=FontSize)
```

```
    plt.ylabel('Angle (degrees)',fontsize=FontSize)
    plt.legend(loc='lower right')
    for label in ax.get_xticklabels()+ax.get_yticklabels():
        label.set_fontsize(TickSize)


#======== End plot of fit data

moment_list=np.hstack((np.arange(-6,.5,.05),np.arange(.75,7.25,.05)))

results={}
for cond in Conditions:
    results[cond]={}
    results[cond]['loading']={}
    results[cond]['unloading']={}
    for level in Levels:
        Tu,Au,Td,Ad,mn,mx=Constants[cond][level]

        results[cond]['loading'][level]=evaleq(moment_list,[Tu,Au,mn,mx])
        results[cond]['unloading'][level]=evaleq(moment_list,[Td,Ad,mn,mx])

actual={}

for cond in Conditions:
    actual[cond]={}
    actual[cond]['loading']={}
    actual[cond]['unloading']={}
    for level in Levels:
        upswing,downswing=FindSwing(Data[cond][level]['Moment'],
                                    Data[cond][level]['Angle'])
```

```
        actual[cond]['loading'][level]=interp(moment_list,upswing[0],upswing[1])
        actual[cond]['unloading'][level]=interp(moment_list,
        downswing[0],
        downswing[1])

#===Plot data

#== Global stiffness
def plotglobal():
    colors = ['-.r','g',':b','--y']
    fig = plt.figure()
    ax=fig.add_subplot(111)
    plt.hold(True)
    for cond,color in zip(Conditions,colors):
    #for cond in Conditions:
        grm=actual['Intact']['loading']['L34']+results[cond]['loading']['L45']+\
        actual['Intact']['loading']['L51']
        gra=actual[cond]['loading']['L34']    +actual[cond]['loading']['L45'] +\
        actual[cond]['loading']['L51']
        plt.plot(moment_list,grm,color,label=cond)
        #plt.plot(moment_list,grm,'--r',label='PRBM')
        #plt.plot(moment_list,gra,'b',label="Measured")
        grm=actual['Intact']['unloading']['L34']+\
        results[cond]['unloading']['L45']+actual['Intact']['loading']['L51']
        gra=actual[cond]['unloading']['L34']+\
        actual[cond]['unloading']['L45']+actual[cond]['unloading']['L51']
        plt.plot(moment_list,grm,color)
        #plt.plot(moment_list,grm,'--r')
        #plt.plot(moment_list,gra,'b')
```

```
        plt.legend(loc='lower right')
        plt.title("Multilevel moment-rotation response ("+cond+")",
                  fontsize=FontSize)
        plt.xlabel("Moment (Nm)",fontsize=FontSize)
        plt.ylabel("Angle (degrees)",fontsize=FontSize)
        plt.ylim((-10,20))
        plt.xlim((-8,8))
    for label in ax.get_xticklabels()+ax.get_yticklabels():
        label.set_fontsize(TickSize)
        #plt.title("Multilevel moment-rotation response ( L3-S1)")

#plt.show()

#== End Plot Gloabal

#=====

def Cadence(cond,lev,swing='loading'):
    grm=   results['Intact'][swing]['L34']   +results[cond][swing]['L45']   +\
    results['Intact'][swing]['L51']

    if swing=='loading':
        grmm=   min(results['Intact'][swing]['L34'])   +\
        min(results[cond][swing]['L45'])   +min(results['Intact'][swing]['L51'])

    if swing=='unloading':
        grmm=   max(results['Intact'][swing]['L34'])   +\
        max(results[cond][swing]['L45'])   +max(results['Intact'][swing]['L51'])

    grm= grm-grmm
```

```
if swing ==’loading’:

    if lev ==’L45’:
        temp=results[cond][swing][lev]-min(results[cond][swing][lev])
        cadm=temp/grm
    else:
        temp=results[’Intact’][swing][lev]-min(results[’Intact’][swing][lev])
        cadm=temp/grm

    gra=actual[cond][swing][’L34’]          +actual[cond][swing][’L45’]   +\
    actual[cond][swing][’L51’]
    gram=min(actual[cond][swing][’L34’])          +\
    min(actual[cond][swing][’L45’])   +min(actual[cond][swing][’L51’])
    gra=gra-gram

    temp=actual[cond][swing][lev]-min(actual[cond][swing][lev])
    cada=temp/gra

if swing==’unloading’:

    if lev ==’L45’:
        temp=results[cond][swing][lev]-max(results[cond][swing][lev])
        cadm=temp/grm
    else:
        temp=results[’Intact’][swing][lev]-max(results[’Intact’][swing][lev])
        cadm=temp/(grm)

    gra=actual[cond][swing][’L34’]          +actual[cond][swing][’L45’]   +\
    actual[cond][swing][’L51’]
```

```
        gram=max(actual[cond][swing]['L34'])          +\
        max(actual[cond][swing]['L45'])   +max(actual[cond][swing]['L51'])
        gra=gra-gram
        temp=actual[cond][swing][lev]-max(actual[cond][swing][lev])
        cada=temp/gra

    #plt.plot(sg(moment_list[3:]),sg(cadm[3:]*100),'--r',label='PRBM')
    #plt.plot(sg(moment_list[3:]),sg(cada[3:]*100),'b',label="Measured")
    plt.plot(moment_list[3:],cadm[3:]*100,marker,label=cond)
    #plt.title(lev+ ' as percent of total motion ('+cond+")",fontsize=FontSize)
    plt.xlabel('Moment (Nm)',fontsize=FontSize)
    plt.ylabel('Motion (%)',fontsize=FontSize)
    plt.legend(loc='lower right')
    plt.title(lev+ ' as percent of total motion',fontsize=FontSize)
    plt.ylim((0,60))
#

def CadenceBar(cond,moment_load,swing='loading'):
    Measured=[]
    Predicted=[]
    breaknum=(moment_load<0).nonzero()[-1][-1]+1
    flex_load=moment_load[breaknum :]
    ext_load=moment_load[:breaknum]

    for lev in Levels:
        upswing,downswing=FindSwing(Data[cond][lev]['Moment'],
                                    Data[cond][lev]['Angle'])
        if lev=='L45':
            #If it is the operative level constants
            Tu,Au,Td,Ad,mn,mx=Constants[cond][lev]
```

```
    else:
        #If not use the FD constants from the intact case
        Tu,Au,Td,Ad,mn,mx=Constants['Intact'][lev]

    if swing =='loading':
        neut=interp(0,downswing[0],downswing[1])
        ext=interp(ext_load,downswing[0],downswing[1])-neut

        neut=interp(0,upswing[0],upswing[1])
        flex=interp(flex_load,upswing[0],upswing[1])-neut

        Measured.append(list(ext)+list(flex))

        flex=evaleq(flex_load,[Tu,Au,mn,mx])-evaleq(0,[Tu,Au,mn,mx])
        ext=evaleq(ext_load,[Td,Ad,mn,mx])-evaleq(0,[Td,Ad,mn,mx])

    else:
        neut=interp(0,upswing[0],upswing[1])
        ext=interp(ext_load,upswing[0],upswing[1])-neut

        neut=interp(0,downswing[0],downswing[1])
        flex=interp(flex_load,downswing[0],downswing[1])-neut
        Measured.append(list(ext)+list(flex))

        flex=evaleq(flex_load,[Td,Ad,mn,mx])-evaleq(0,[Td,Ad,mn,mx])
        ext=evaleq(ext_load,[Tu,Au,mn,mx])-evaleq(0,[Td,Ad,mn,mx])

    Predicted.append(list(ext)+list(flex))
return Measured,Predicted
```

```
def CadAngle(cond,angles,swing='loading'):
    #Pseudo Code
    moment_load=np.arange(-7.5,7.5,.05)
    Measured,Predicted=CadenceBar(cond,moment_load,swing)

    GSM=0.0
    GSP=0.0

    for level in Measured:
        GSM+=np.array(level)
    for level in Predicted:
        GSP+=np.array(level)

    if angles.max()>=GSM.max() or angles.min()<=GSM.min():
        print "Input angles out of range for Measured",GSM.max(),GSM.min()
    if angles.max()>=GSP.max() or angles.min()<=GSP.min():
        print "Input angles out of range for Predicted",GSP.max(),GSP.min()

    moments_m=interp(angles,GSM,moment_load)
    Measured,Junk=CadenceBar(cond,moments_m,swing)
    moments_p=interp(angles,GSP,moment_load)
    Junk,Predicted=CadenceBar(cond,moments_p,swing)
    return Measured,Predicted

def plotCadAngleCenter(cond,angles,swing='loading'):
    Measured,Predicted=CadAngle(cond,angles,swing)
    width=.75

    fig = plt.figure()
    ax = fig.add_subplot(111)
```

```
    rects1 = ax.bar(angles-width/2,
                    Measured[0],
                    width, color='r',bottom=-np.array(Measured[1])/2.0+\
                                          -np.array(Measured[0]))
    rects2 = ax.bar(angles-width/2,
                    Measured[1],
                    width, color='g',bottom=-np.array(Measured[1])/2)
    rects3 = ax.bar(angles-width/2,
                    Measured[2],
                    width, color='b',bottom=np.array(Measured[1])/2)

    pred1 = ax.bar(angles+width/2,
                   Predicted[0],
                    width, color='r',bottom=-np.array(Predicted[1])/2-\
                                                np.array(Predicted[0]))
    pred2 = ax.bar(angles+width/2,
                   Predicted[1],
                    width, color='g',bottom=-np.array(Predicted[1])/2)
    pred3 = ax.bar(angles+width/2,
                   Predicted[2],
                    width, color='b',bottom=np.array(Predicted[1])/2)

    plt.xlabel('Global Angle (degrees)')
    plt.ylabel('Angle (degrees)')
    plt.title('Global motion of L3-S1 as a function of local motion ('+cond+')')

def plotCadAngle(cond,angles,swing='loading'):
    Measured,Predicted=CadAngle(cond,angles,swing)
    width=1.0
```

```
fig = plt.figure()
ax = fig.add_subplot(111)

rects0=ax.bar(-.5,
              .0,
              width, color='1',)

rects1 = ax.bar(angles-width,
                Measured[0],
                width, color='0.75',)
rects2 = ax.bar(angles-width,
                Measured[1],
                width, color='0.25',bottom=np.array(Measured[0]))
rects3 = ax.bar(angles-width,
                Measured[2],
                width, color='0.5',bottom=np.array(Measured[0]) +\
                                          np.array(Measured[1]))
pred0=ax.bar(-.5,
              .0,
              width, color='1',hatch="/")

pred1 = ax.bar(angles,
               Predicted[0],
                width, color='0.75',hatch="/")
pred2 = ax.bar(angles,
               Predicted[1],
                width, color='0.25',bottom=np.array(Predicted[0]),
                hatch="/")
pred3 = ax.bar(angles,
```

```
                Predicted[2],
                 width, color='0.5',bottom=np.array(Predicted[0]) +\
                                        np.array(Predicted[1]),
                 hatch="/")
    height=np.array(Predicted[0])+np.array(Predicted[1])+np.array(Predicted[2])

    plt.xlabel('Global Angle (degrees)',fontsize=FontSize)
    plt.ylabel('Angle (degrees)',fontsize=FontSize)
    plt.title('Global and local motion of L3-S1 ('+cond+')',fontsize=FontSize)
    for label in ax.get_xticklabels()+ax.get_yticklabels():
        label.set_fontsize(TickSize)
    l1=ax.legend((rects1[0], rects2[0],rects3[0]), ('L5-S1', 'L4-L5','L3-L4'),
              loc='lower right')
    l2=ax.legend((rects0[0], pred0[0]), ('Measured', 'PRBM'),
              loc='upper left',fancybox=False)
    l2.draw_frame(False)
    plt.gca().add_artist(l1)
    plt.xlim((-9.5,12.5))
    plt.ylim((-9,12))


#    addlabels=[pred1,pred2,pred3]
#    for rects in addlabels:
#        # attach some text labels
#        for rect in rects:
#            height = rect.get_height()
#            if height>=1.2:
#                ax.text(rect.get_x()+rect.get_width()/2, 0.5*height, '%.*f'%(1,
#                        float(height)),ha='center', va='bottom',
#                        rotation='vertical')
```

```
def plotCad(cond,moment_load):
    Measured,Predicted=CadenceBar(cond,moment_load)
    width = .75     # the width of the bars

    fig = plt.figure()
    ax = fig.add_subplot(111)

    rects1 = ax.bar(moment_load-width/2,
                    Measured[0],
                    width, color='r',)
    rects2 = ax.bar(moment_load-width/2,
                    Measured[1],
                    width, color='g',bottom=Measured[0])
    rects3 = ax.bar(moment_load-width/2,
                    Measured[2],
                    width, color='b',
                    bottom=np.array(Measured[0])+np.array(Measured[1]))

    pred1 = ax.bar(moment_load+width/2,
                   Predicted[0],
                    width, color='r',)
    pred2 = ax.bar(moment_load+width/2,
                   Predicted[1],
                    width, color='g',bottom=Predicted[0])
    pred3 = ax.bar(moment_load+width/2,
                   Predicted[2],
                    width, color='b',
                    bottom=np.array(Predicted[0])+np.array(Predicted[1]))
```

```
    plt.xlabel('Moment (Nm)')
    plt.ylabel('Angle (degrees)')
    plt.title('Global motion of L3-S1 as a function of local motion ('+cond+')')

def plotComp(Conditions,mark,angles):
    numcond=len(Conditions)
    width=2.2/numcond
    fig=plt.figure()
    ax = fig.add_subplot(111)

    ind=0
    axlegend=[]
    for cond,hatchmark in zip(Conditions,mark):
        Measured,Predicted=CadAngle(cond,angles)
        print cond
        pred0=ax.bar(-.25,
                     .0,
                      width, color='1',hatch=hatchmark)
        pred1 = ax.bar(angles-numcond*width/2.0+ind*width,
                       Predicted[0],
                       width, color='0.75',hatch=hatchmark)
        pred2 = ax.bar(angles-numcond*width/2.0+ind*width,
                       Predicted[1],
                       width, color='0.25',bottom=Predicted[0],
                       hatch=hatchmark)
        pred3 = ax.bar(angles-numcond*width/2.0+ind*width,
                       Predicted[2],
                    width, color='0.5',bottom=np.array(Predicted[0])+\
                    np.array(Predicted[1]),
                    hatch=hatchmark)
```

```
        ind+=1
        axlegend.append(pred0[0])
        if cond=='Intact':
            leg1=pred1
            leg2=pred2
            leg3=pred3
    plt.xlabel('Global Angle (degrees)',fontsize=FontSize)
    plt.ylabel('Angle (degrees)',fontsize=FontSize)
    plt.title('Global and local motion of L3-S1 ('+cond+')',fontsize=FontSize)
    l1=ax.legend((leg1[0], leg2[0],leg3[0]), ('L5-S1', 'L4-L5','L3-L4'),
              loc='lower right')
    l2=ax.legend(axlegend,Conditions,loc='upper left')
    l2.draw_frame(False)
    plt.gca().add_artist(l1)
    plt.xlim((-9.5,11.5))
    plt.ylim((-9,11))
    for label in ax.get_xticklabels()+ax.get_yticklabels():
        label.set_fontsize(TickSize)



#plotCad('Intact',np.array([2,4,6,8]))
#plotCad('FlexBAC',np.array([2,4,6,8]))
#plotComp(['Intact','FlexBAC','Charite'],np.array([-8,-6,-4,-2,2,4,6,8]))
angle_list=np.array([-8,-5,-2,2,4.5,7.5,10])
#plotCadAngle('Intact',angle_list)
#plotCadAngle('Fused',angle_list)
#plotCadAngle('FlexBAC',angle_list)
plotComp(['Intact','Fused','Charite','FlexBAC'],['','//','/','\\'],angle_list)
plt.show()
```